Polar Science 42 (2024) 101106

Contents lists available at ScienceDirect

Polar Science

journal homepage: www.elsevier.com/locate/polar

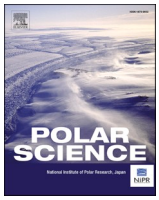

A statistical study of precipitation on the eastern antarctic plateau (Dome-C) using remote sensing and in-situ instrumentation

Massimo Del Guasta [a,*], Philippe Ricaud [b], Claudio Scarchilli [c], Giuliano Dreossi [d]

[a] National Institute of Optics (INO) CNR, Via Madonna Del Piano 10, 50019, Sesto Fiorentino, Firenze, Italy
[b] CNRM, Meteo France, CNRS, UMR 3589, 42 Av. G. Coriolis, 31057, Toulouse Cedex, France
[c] Laboratory for Observations and Measurements for Environment and Climate (SSPT-PROTER-OEM), ENEA, Rome, 00123, Italy
[d] Department of Environmental Sciences, Informatics and Statistics, Cà Foscari University of Venice, Italy

ARTICLE INFO

Keywords:
Ice precipitation
lidar
icecamera
Antarctica
Polar Clouds

ABSTRACT

Studying precipitation at very high latitudes is a challenge, particularly during the polar winter. Direct monitoring of ice habit and size in high latitude precipitation is crucial for validating the algorithms used to derive precipitation from radar, and for improving the climatological modeling of polar areas. The high plateau lacks long-term direct observations of precipitation. In this work, carried out at Concordia Station (Dome-C (DC), −75°S, 123°E, 3233 m a.m.s.l), the use of a depolarization LIDAR, a flatbed scanner (ICECAMERA), a microwave profiler (HAMSTRAD) and meteorological instrumentation made possible the study, over the period 2014–2021, of shape, size, height and temperature of formation of precipitation. The precipitation sources were classified into four types: ice fogs, liquid fogs, mixed-phase clouds, and cirrus. Ten representative ice habits for Dome-C were chosen. The size distribution for every habit was calculated, allowing for the estimation of the corresponding radar reflectivity. The use of W-band radars, such as CLOUDSAT, with a sensitivity of −28dB, resulted in capturing all the crystals observed in Concordia. A positive trend was observed between grain size and height in ice habits that are typical of cloud precipitation. North West (NW) and North East (NE) winds at cloud height, blowing from coastal regions, caused the majority of precipitation from clouds. The study also examined the height trend of the ice habit composition of precipitation. The ice habit composition for each of the four types of precipitation source was analyzed, and the possibility of determining the source by simply observing the precipitation was explored. This work marks the first comprehensive investigation of precipitation on the eastern Antarctic plateau.

1. Introduction

The study of inland Antarctic ice precipitation is a challenge due to the harsh environmental conditions that limit outdoor activity by humans and instrumentation (Genthon et al. ,2016). It can only be achieved in a few permanently manned stations. In situ measurements of precipitation are thus rare in this polar area, are performed manually (Stenni et al., 2016), and can be affected by large uncertainties. On the high plateau, this is especially true, where snow accumulates every year for less than 20 cm of snow depth (Palerme et al., 2014). Thus, the global precipitation products that depend on these observations [i.e. the Global Precipitation Climatology Centre (GPCC) (Schneider et al., 2017),] do not cover this region.

Across Antarctica, ice accumulates from light snowfall episodes, which frequently fall as near-continuous clear-sky precipitation ("Light snow", LS, or "diamond dust", DD), (Walden et al., 2003; Fujita and Abe, 2006). However, there are also relatively short-lived intrusions of maritime air giving heavier precipitation, which are often in the form of extreme precipitation events (EPEs), occurring during periods of strong meridional flow when the mid-tropospheric planetary waves are amplified (Hirasawa et al., 2000; Genthon et al., 2016). These events contribute to approximately 40% of the annual DC precipitation (Scarchilli et al., 2011; Turner et al., 2019). The contribution of DD to total snow deposition is still uncertain due to its close proximity to the surface and the inability of satellite-borne instruments to measure it. DD may be responsible for discrepancies in precipitation retrievals between remote-sensing platforms and in-situ observations, and between model-based predictions and in situ–based observational analysis results

* Corresponding author.
E-mail address: massimo.delguasta@ino.cnr.it (M. Del Guasta).

https://doi.org/10.1016/j.polar.2024.101106
Received 7 December 2023; Received in revised form 23 July 2024; Accepted 8 August 2024
Available online 12 August 2024

(Gultepe et al., 2017).

The satellite-borne Cloud Profiling Radar (CPR) of CloudSat (Liu, 2008) provided a quantum leap in observing precipitation in the Antarctic atmosphere (poleward to 82°S). CPR data is used to replace ground-based information that is missing, particularly in Antarctica, where any method of studying precipitation is challenging. However, CPR data are not reliable below 700 m above ground (Stephens et al., 2008) and with a too loose time resolution in order to catch the entire evolution of each single event (Souverijns et al., 2018), and are not sensitive to optically thin clouds (optical depth 0.1–0.4) (Stephens et al., 2002). Being a single-frequency radar, the retrieval of precipitation quantities from CPR relies on many assumptions about the properties of particles, resulting in ≈50% uncertainties for Ice Water Content (IWC) (Heymsfield et al., 2008). The most significant cause of uncertainty in retrieving IWC and snowfall rate is the microphysical assumptions (shapes and size distribution of particles) (Hiley et al., 2011; Wood et al., 2015; Kou et al., 2023). Radar reflectivity is proportional to the 6th power of the size of ice crystals, as particles are small relative to the radar wavelength. LIDAR is more sensitive to small ice particles than radar because of the shorter wavelength and a backscatter proportional to the second power of particle size. Merging Cloud Profiling Radar data with cloud-aerosol LIDAR (CALIOP) data (Winker et al., 2003, 2007) into RL-GeoProf (Mace et al., 2009) and *2C-ICE* (Deng et a.,2015) improved the quality of the Cloudsat products and extended the information close to the ground, even if matching the two different resolutions, footprints, and pointing directions is still challenging. Listowski et al. (2019) worked on a similar data set (DARDAR, including also MODIS data) specifically in the Antarctic region.

Modeling of hydrometeors is still necessary to extract IWC, precipitation rate, and ice particle information from either CPR (Austin et al., 2009) or CALIOP (Avery et al., 2012). The models obtained from intensive mid-latitude field campaigns are not guaranteed to be valid in polar regions. The direct observation of the habit and size of precipitation, other than necessary for understanding precipitation processes on the Antarctic plateau, is therefore also required for validating precipitation models, CloudSat and other radar retrieval algorithms in this extreme environment (Lemonnier et al., 2019).

Antarctica's snow particles are typically smaller than those found in other regions of the world. Only near the coast, where more water vapor is available, are large particles found, and their size and shapes are similar to those of mid-latitude particles (Konishi et al., 1992; Grazioli et al., 2017b). Snowflakes of varying sizes are recorded at inland stations, with particles ranging from less than 100 μm at the South Pole (Walden et al., 2003; Lawson et al., 2006) to hundreds of μm at other inland stations (Lachlan-Cope et al., 2001).

The observation of ice particles in inner Antarctica requires imaging techniques with a resolution of a few microns. Photographic studies of precipitation in the Antarctic interior are rare and were primarily conducted at the South Pole Station (SP) using formvar replicas. In his early work with formvar, Hogan (1975) identified millimeter-sized columnar crystals and column- and bullet-rosettes in cloud precipitation, and smaller plate-like particles in clear-sky precipitation. Satow (1983) utilized formvar replicas on the Mizuho plateau and found that single bullets and combinations of bullets were common. Long solid column crystals were also found with a mean length of 290 μm. Small (50–400 μm) hexagonal, triangular, scalene and square plates were also observed. Kikuchi and Hogan (1979) collected formvar replicas of DD in the summer at SP, finding columnar crystals of 90 μm average lengths and plates as small as 50 μm in diameter. Ohtake and Yogi (1979) categorized Antarctica's winter ice crystal precipitation into six categories. These included large rosettes, bullets and columns (mm-sized), thin hex plates and columns (200 μm diameter or less), and smaller crystals of various shapes including triangular and polyhedral. Smiley et al. (1980) reported size distributions of Antarctic DD in winter and spring for particles larger than 50 μm. They observed the same ice crystal forms that were reported earlier. Walden et al. (2003) studied DD, blowing snow, and cloud precipitation in winter, at SP, by collecting crystals on slides and analyzing them using microphotography. Their study revealed columns with an average length of 60 μm and plates with an average diameter of 30 μm in DD. A similar technique was used by Kameda et al., 2007) at Dome Fuji, throughout the year 2003. Their main observation was rosettes and columns (from compact to elongated), and their median sizes were 500 and 430 μm, respectively.

The typical method for observing ice precipitation on the plateau was to use formvar replicas and/or microphotography, but these techniques take time, are difficult to implement throughout the year and are often limited to short field campaigns and samples of very limited size.

Designing automatic instruments for the photographic study of precipitation in such a harsh environment necessarily requires a compromise between the high resolution of microphotography and the low resolution but robustness of outdoor optical instruments (such as disdrometers). Lawson et al. (2006) worked at SP in the summer by using Cloud Particle Imagers (CPIs), which replaced formvar replicas. This technique made it possible to analyze nearly 700,000 crystal images automatically for size, aspect ratio, and other shape parameters. An automatic classification software, based on shape parameters, was used to categorize the images into nine simplified classes. However, there is still a lack of direct information about ice precipitation in the interior of Antarctica, particularly during the coldest months.

The Concordia international station, situated on the Dome-C (DC), 75°S, 123°E, at 3220 m of altitude, is a special location for testing new instrumental setups for precipitation studies. Summer temperatures are below −25 °C, while winter temperatures can reach −85 °C. The 3 m average wind speed is 3 ms^{-1} (Aristidi, 2005). DC can be considered as 'inside' ice clouds if DD is formed, or inside the precipitation trail ('virga') if there are cirrus or altocumulus clouds present. Santachiara et al. (2016) used scanning electron microscopy (SEM) to carry out detailed work on a few individual DD and cloud precipitation crystal replicas in DC. They also analyzed very small particles (10–50 μm), in a size range that is inaccessible to conventional photographic methods. Daily photographs are taken manually of the snow that is collected on horizontal benches in DC. However, at present, no comprehensive analysis of precipitation microphysics has been conducted.

In DC, precipitation was automatically photographed, sized, and classified by a flatbed scanner (ICECAMERA) in the last decade (Del Guasta, 2022a). Since 2012, an automated depolarization LIDAR has been in operation from nearly ground level to 7000 m height. Profiles of tropospheric temperature are provided by a microwave radiometer. The combination of these instruments enabled the first systematic study of precipitation size and morphology on the eastern Antarctic plateau. This paper is the first one to describe the results, and it will proceed as follows: Section 2 describes instrumentation and methodology used in order to highlight ice habit, precipitation sources and the snow height of formation. Sections 3.1 to 3.3 describe the thermodynamics conditions associated with different precipitation sources and ice habits. Section 3.4 analyzes the size distributions of different ice habits and estimates their radar reflectivity for different radar types. In Section 3.5, the relationship between size and height for various ice habits is investigated. In Section 3.6, the differences in ice habit composition among the different precipitation sources are discussed, and a method is being evaluated for determining the source type by directly observing ice habits on the ground.

2. Methods

2.1. The instruments

The instrumental setup is located in the shelter 'Physics', which is approximately 500 m south of Concordia Station and is statistically always upwind with respect of the emissions from the main station. The instrumental setup is organized as follows.

2.1.1. ICECAMERA

ICECAMERA is a flatbed scanner that is specifically made for directly observing and measuring precipitation in the harsh environmental conditions of DC (fully described in Del Guasta, 2022a). The principle is simple: at low temperatures and low wind speeds, precipitation falling over a flat glass surface accumulates with time. Every hour, before cleaning it, the collecting surface is optically scanned, each individual grain being segmented, measured and classified by means of a Convolutional Neural Network (CNN) into one of 15 classes of 'crystal' shapes (named 'ice habits' in the rest of the paper). The instrument's optical resolution of 17 μm is not sufficient to capture fine details of the particles, and particles smaller than 60 μm are not processed (this selection took apart 7% of the total number of grain detected). Moreover, mainly in summer, the sublimation of smallest particles can result in their undercount (Del Guasta, 2022a).

2.1.2. The depolarization LIDAR

Since 2009, an automatic 532 nm depolarization LIDAR designed and built by Istituto Nazionale Ottica (INO CNR) has been operating at DC (http://lidarmax.altervista.org/englidar/Antarctic%20LIDAR.php). Appendix A describes the characteristics of the instrument. In 2013, the LIDAR became reliable after experiencing several issues related to the low pressure and humidity. The instrument provides vertical profiles of raw backscatter signal and depolarization from ~10 m up to ~7000 m a.g.l. This height range covers the majority of DC tropospheric clouds (Bromwich et al., 2012). The system is a simple 532 nm elastic-backscatter LIDAR, that permits the discrimination of the phase of water by means of the depolarization ratio (δ), that is, the intensity ratio between the planes of polarization parallel and orthogonal to that of the linearly polarized laser source.

δ is a key tool for the distinction between solid and liquid suspended particles, as it relies on a basic symmetry rule in electromagnetics: only particles with spherical or cylindrical symmetry around the LIDAR axis do not depolarize in the backscatter (Sassen,1991; Del Guasta et al., 2012). Liquid particles are spherical and thus non depolarizing, but also horizontally oriented large crystals (which are not uncommon at mid-latitudes (Platt, 1977; Sassen,1999), are shown to produce high LIDAR backscattering and low depolarization ratio ($\delta < 0.1$) similar to that of liquid particles. To avoid any ambiguity, the LIDAR axis in DC is tilted ≈5° off-zenith. The cylindrical symmetry of oriented plates is broken by doing this (Saito and Yang, 2016), and liquid particles are the only ones that do not depolarize. A second aspect to consider when using δ as a tool for water-phase discrimination is the possible effect of multiple scattering, a phenomenon which introduces depolarization also in liquid clouds. This effect is visible as an almost linear increase in δ with the penetration of the cloud (Hu et al., 2006). With Field of View of the DC LIDAR (Appendix A) and the small optical thickness of the local liquid clouds, this effect was observed to be limited to <15% maximum depolarization at the cloud top. The classification of the layer as 'liquid' does not exclude the presence of ice particles within it, as the cloud liquid signal simply overwhelms any ice signal. As LIDAR depolarization ratio we used in this work the 'total' depolarization:

$$\delta = K\ Vs\ Vp^{-1} \quad (1)$$

where V is the LIDAR signal that has been offset-subtracted, and -p and -s refer to perpendicular and parallel components respectively. K is the ratio of the two overall gains for the -p and -s photomultipliers and digitizer chains. A possibly problematic aspect affecting the use of total depolarization is its dependency on the optical depth of the cloud: subvisual clouds can show a low total depolarization because the molecular air contribution to the -p signal is important. In DC, we only considered layers showing a scattering ratio (R = cloud signal/air signal) larger than $R \approx 3$.

2.1.3. HAMSTRAD

HAMSTRAD is a microwave radiometer that profiles temperature, water vapor (H_2O), and liquid water above DC, measuring at both 60 GHz (O_2 line to deduce the temperature) and 183 GHz (H_2O line). The radiometer was installed in 2009 (Ricaud et al., 2010a; and b). HAMSTRAD allows the retrieval of the vertical profiles of temperature and water vapor from the ground to 10-km height with vertical resolutions of 30–50 m in the Planetary Boundary Layer (PBL), and 100 m in the free troposphere. The estimated rms error of temperature is 0.25 K in the PBL, 0.5 K in the free troposphere and 1 K in the upper troposphere (Ricaud et al., 2014). The 60-GHz line is not sensitive to ice, to vapor or to liquid water. Even if precipitations are present, they do not interfere with the 60-GHz signal. Accumulations of snow/ice on the dome that protects the radiometer at DC have not been shown to impact the temperature retrievals.

On average, in the PBL, HAMSTRAD temperatures tend to be consistent to ±1 K with the temperatures from radiosondes, space-borne observations and meteorological reanalysis, and cold-biased by 1–3 K between 1 and 5 km a.g.l. (Ricaud et al., 2014). The time resolution ranges from 1 to 7 min, which allows for detection and analysis of atmospheric processes such as the diurnal evolution of the PBL (Ricaud et al., 2012). In the present work, only HAMSTRAD temperature data were used to estimate the temperature at the height of precipitation formation.

2.1.4. Meteorological data

Since 2005, vertical profiles of Temperature, Pressure, Relative Humidity, Wind Speed and Direction have been retrieved from radiosonde data, launched once per day at 12:00 UTC by the Institut Polaire Français Paul Emile Victor – IPEV/Italian Antarctic Meteo-Climatological Observatory, (http://www.climantartide.it). The same meteorological parameters are sampled hourly at 2 m a.g.l. by an automatic weather station managed by the Italian Meteo-Climatological Observatory and located a few hundred meters southwest of the Concordia base (http://www.climantartide.it). In this work, wind speed and direction were derived for the height of precipitation formation from the 12:00 UTC balloon sounding, and were assumed to be representative for the entire day.

2.2. Methods of data analysis

A pre-analysis of the entire dataset was necessary in order to identify and reject invalid data from ICECAMERA and LIDAR. Any ICECAMERA scans that were out of focus or showed thick snow or frost covering the detection surface were deleted (approximately 20% of total scans). LIDAR data showing a too weak signal due to snow/frost cover of the telescope or laser weakness were disregarded (approximately 15% of total). After this screening, in the first analysis LIDAR false color plots were manually processed in order to determine the type of cloud layer originating the precipitation observed in each ICECAMERA scan. The plots were also visually analyzed to estimate the 'Height Of Formation' (HOF) of precipitation. Once the HOF has been estimated, HAMSTRAD data was interpolated to obtain the temperature at HOF (TOF). Additionally, the daily 12:00 UTC radiosounding data was utilized to qualitatively estimate the typical wind direction and humidity at the HOF for different cloud types. The local meteorological station provided data at the surface.

Each ICECAMERA scan was automatically segmented into ice grains, and each grain was analyzed for size and shape. As a result of the process, each ice grain corresponds to a data vector including time of observation, size and shape parameters, probabilities of CNN classification, type of originating cloud, HOF, TOF, surface meteo conditions (temperature, RH, wind), PTU data (12:00 UTC) (temperature, RH, wind) at HOF. These vectors (available at https://zenodo.org/doi/10.5281/zenodo.8427613 (Del Guasta and Ricaud, 2023) were finally, statistically analyzed. The analyzed dataset, as well as all statistics and

figures in this work, cover the period of January 2014 to December 2021.

2.2.1. Classifying and measuring ice particles in ICECAMERA scans

As described in Del Guasta (2022a) ICECAMERA scans are segmented into images of individual grains. Each grain is measured in terms of projected surface, Feret length, Feret width and aspect ratio. The Feret length is assumed as the size (D) of the particle throughout this work. With respect to the original CNN classification scheme (Del Guasta, 2022b) a new class was introduced: 'off-focus' particles. In fact, a first overview of ICECAMERA with the original CNN revealed the misclassification as 'plates' or 'spheroidal particles' of many 'off-focus' particles. The Confusion Matrix (CM) of the new CNN used in this work (Fig. 1) is very similar to the original one. Most of the 15 'ice classes' have a positive prediction rate of more than 80%. The output of the classifier is a probability vector of Pcnn'$_i$ ($i \in [1,15]$) for the classification into the i-th class.

Only particles classified with a probability of at least 50% (max (Pcnn'$_i$) > 0.5) within the 15 classes were considered to be 'properly classified' and retained in the present work. This selection took a part 28% of the total number of grains initially detected.

Among properly classified habits, 'Trigonal plates' were uncommon (0.3% % of the total number). Furthermore, most particles identified as 'trigonal plates' resulted a casual assembly of columnar crystals into triangular shapes. 'Clusters', even if they were common (11% of total), were caused by the random overlap of ice crystals on the glass surface during heavy precipitation events, while 'fibers' (0.2%), 'frost' (2%) and 'off-focus' (13%) were undesired artefacts. Particles classified as 'fiber', 'cluster', 'frost', 'trigonal plates', and 'off-focus', which made up 27% of the total, were therefore disregarded in the statistical analysis. As a consequence, just 52% of the particles that were first identified by ICECAMERA and only 10 ice habits were preserved in the statistics. Only the probabilities Pcnn'$_i$ ($i \in [1,10]$) for the subset of the ten selected ice habits (Fig. 2) were used in the statistics. Pcnn'i was finally re-normalized to unity (Pcnn $i = |$ Pcnn'$_i$ ($i \in [1,10]$)$|$).

2.2.2. Identifying the layer that generates precipitation

The depolarization LIDAR was used as a tool to discriminate the phase of the precipitation-producing layer at the time of ICECAMERA scans, and for estimating the height of formation (HOF) of the precipitation. No special data processing is required for these simple tasks, Time-Height-Signal (THS) and Time-Height-Depolarization (THD) false color plots are sufficient. By utilizing these plots (Fig. 3), we categorized the layers causing precipitation into four Precipitation Types (PT) as follows.

2.2.2.1. Cirrus. This class encompasses all clouds that are completely frozen and typically have a top above 500 m a.g.l. The unique feature of DC is that at ground level we are inside the precipitation trail of cirrus, and collecting precipitation is almost equivalent to flying-sampling under a mid-latitude cirrus. In LIDAR plots, cirrus are easily spotted because their precipitation trails show a vertical continuity in THD plots, with δ often higher than 30% (Fig. 3a). During the fall, depolarization is usually constant, which indicates the absence of melting regions and/or significant changes in crystal habit. LIDAR is more sensitive than the naked eye in detecting ice clouds (McFarquhar et al., 2000).

2.2.2.2. Mixed-phase clouds. In this type of cloud, typically higher than 100 m a.g.l., a thin liquid layer ($\delta \ll 15\%$) a few hundred meters thick, originates ice precipitation ($\delta > 15\%$). An example is shown in Fig. 3b after 6:00 UTC. A strong LIDAR signal with $R > 100$ is coupled with very low δ, inside the liquid layer. Supercooled layers are not uncommon in DC during the summer (Ricaud et al., 2024). For the purpose of this work, we will define as 'clouds' the ensemble of 'cirrus' and 'mixed-phase clouds'.

2.2.2.3. Ice fog – diamond dust. Ice fog consists of suspended small ice crystals, having similar fall velocities as fog droplets, and that often reduces visibility to less than 1 km in polluted arctic areas. (Gultepe et al.,2014, 2017).

At the remote site of DC, the scarcity of ice nuclei presumably makes homogeneous nucleation (occurring at temperatures near −40 °C) much

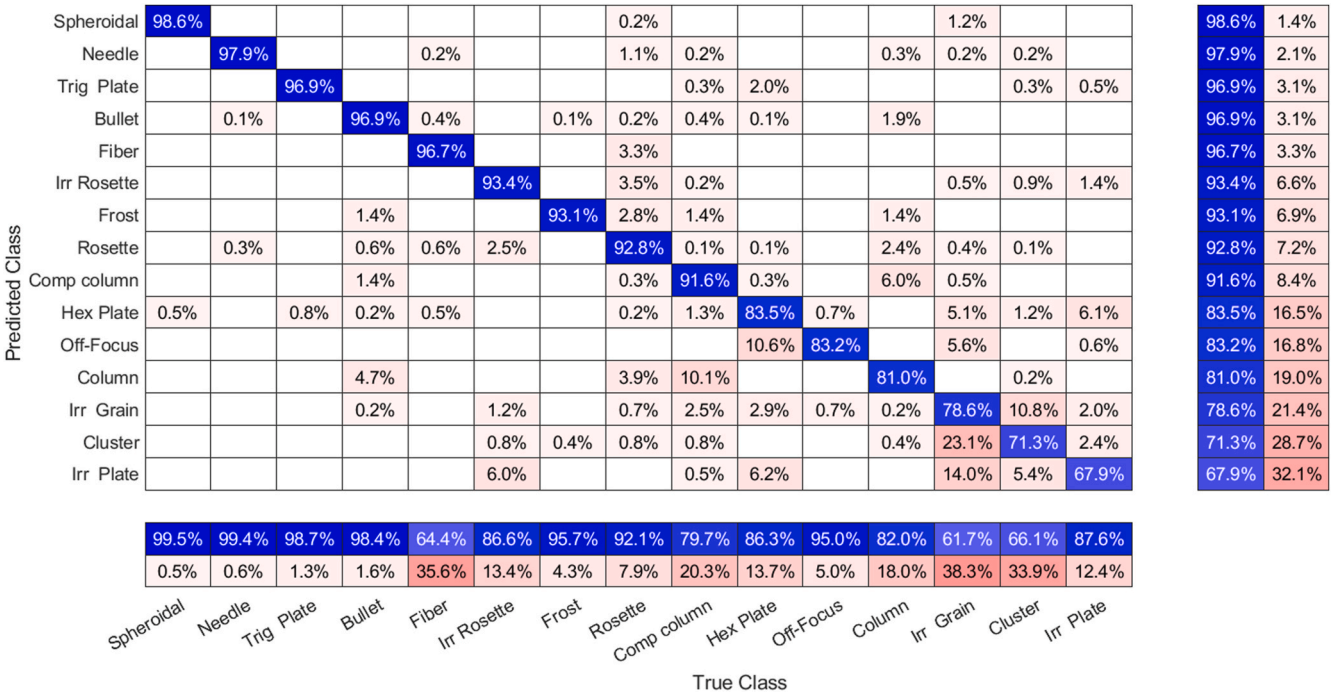

Fig. 1. The confusion matrix for ICECAMERA's CNN. The positive prediction rate displayed in the vertical blue column indicates the probability of correct classification. Positive prediction efficiency is sorted in descending order. (For interpretation of the references to color in this figure legend, the reader is referred to the Web version of this article.)

Ice habit	Typical shape	Number	%
Needle	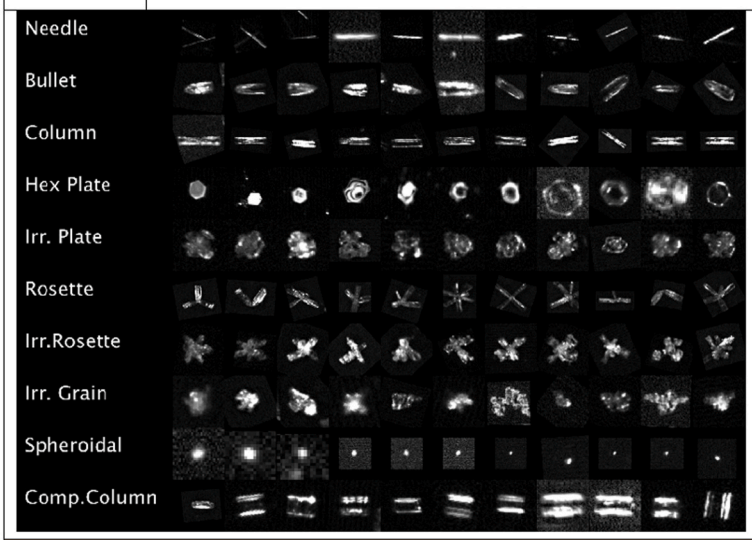	1E5	4.8
Bullet		1.6E5	7.7
Column		1.1E5	5.2
Hex Plate		3.3E5	15.8
Irr. Plate		1.6E5	7.7
Rosette		1.5E5	7.2
Irr.Rosette		1.9E5	9.1
Irr. Grain		2.7E5	13
Spheroidal		1.9E4	0.9
Comp.Column		7.4E3	0.4
Total number of 'properly classified' (10 habits)		1517798	72.3 %
Total number of 'properly classified' (15 habits)		2100405	100 %

Fig. 2. Examples of the ten ice habits adopted in this work. The number of properly classified particles in each habit is shown, along with their relative contribution to the total of properly classified particles (in the 15 classes).

more important than heterogeneous nucleation. The size of typical ice fog particles is less than 200 μm (Gultepe et al., 2020) but it could evolve into larger, precipitating particles: ice fog can produce LS or DD, defined by the WMO as 'precipitation that falls from a cloudless sky in the form of small ice particles'. Ice fog can be regarded as a cirrus cloud forming at the surface. In DC, DD precipitation either originated from persisting ice fogs, or from boundary layer clouds (HOF<100 m) in the form of separate bursts of DD. These events were also labeled as 'ice fog' in this work, as suggested by Gultepe et al. (2020). Detailed work on the formation of ice fogs in DC was performed by Vignon et al. (2022).

Ice fog layers, characterized by high LIDAR depolarization δ >15%) and low signal are often observed in DC in clear-sky conditions, as shown in Fig. 3c. Less than 10% of ice fog particles were collected (not shown) with surface wind directions compatible with some contamination from the DC emissions (N-NE).

2.2.2.4. Liquid fog. Liquid fogs have been observed in the Arctic at temperatures as low as −40 °C (Cox et al., 2019). 'Liquid fogs' are defined in this work as fog layers close to the ground (HOF<100 m a.g.l.) marked by a very weak LIDAR depolarization (δ ≪15%) coupled with a strong signal (R > 50, e.g. Fig. 3d after 12:00 UTC). The low depolarization is a strong marker of the dominating presence of liquid particles (Sec. 2.1.2), but low concentrations of ice particles (such as plates or needles) cannot be excluded, and in fact they are observed as precipitation in ICECAMERA records. Fog bows have been observed in these layers when the Sun is low, in some cases. Liquid fogs are also be generated on the emissions of the local power plant, but our measurement station is almost always upwind from the smokestack. 12% of 'liquid fogs' were observed with surface wind directions (N-NE) compatible with a contamination from the DC emissions. A random cross-check with mercury measurements in air (Magand O., pers. comm.) showed no evidence of Hg from combustion for most of the liquid fog events analyzed in this work.

For the purpose of this work, we will define as 'fog' the ensemble of 'liquid fog' and 'ice fog'.

2.2.2.5. Ambiguous cases. The classification of the origin of precipitation can be ambiguous or impossible in the co-presence of 'fogs' and 'clouds'. The possible seeding of the 'fog' by cloud particles, the possible growth and riming of cloud precipitation within the fog layer, and the masking effect of fog on cloud precipitation in THD plot complicate the problem. In cases of unclear classification (such as Fig. 4) no decision is taken about the type of originating cloud and the HOF. In these cases, ICECAMERA scans are processed for statistical purposes (snow size, habit, etc.), but they are not linked to any cloud type, HOF or TOF. The total number of ICECAMERA scans classified into the different PTs and the total number of ice particles attributed to each PT are summarized in Table 1.

27% of ICECAMERA scans and 21% of ice particles were labeled of 'ambiguous' origin in terms of PT. Ice fogs and cirrus resulted to be the main sources of particles, with a total of 68% of case and 73% of particles. Liquid fog or mixed-phase clouds were attributed to only 8% of scans and 6% of particles (at DC these PTs can be observed only when TOF is above −40 °C).

2.2.3. Estimating the height and temperature at which precipitation forms

LIDAR THD plots are also utilized to estimate the height of formation of the precipitation captured by ICECAMERA. A minimum HOF of 20 m was accepted during the analysis. In the case of 'ice fog' the HOF is assumed to be the top of the layer (Fig. 3c). In 'mixed-phase' layers and 'liquid fogs', it is assumed that the HOF is the top of the liquid layer, as observed in the THS plot (Fig. 3 b). Having neglected ambiguous cases in this analysis (Sec. 2.2.2.5), the possibility that precipitation originates from above is improbable. Assuming HOF to be the top of liquid layers is somehow arbitrary, but there is no way to find out the exact height at which ice forms within a liquid layer, because of the masking effect of the strong backscatter of liquid particles over the weak signal from ice crystals. Cirrus represent a complex case because a consistent delay between ice formation and the collection of particles on the ground can exist. In addition, wind shear can cause different slopes of the cirrus precipitation trail in THD plots. In cirrus, HOF is determined on the THD plot, as shown in Fig. 3a by manually 'back-tracing' the precipitation trail that reaches the ground at the time of ICECAMERA scan, up to the highest height where δ>15% on THD. In the case of high cirrus, the THD

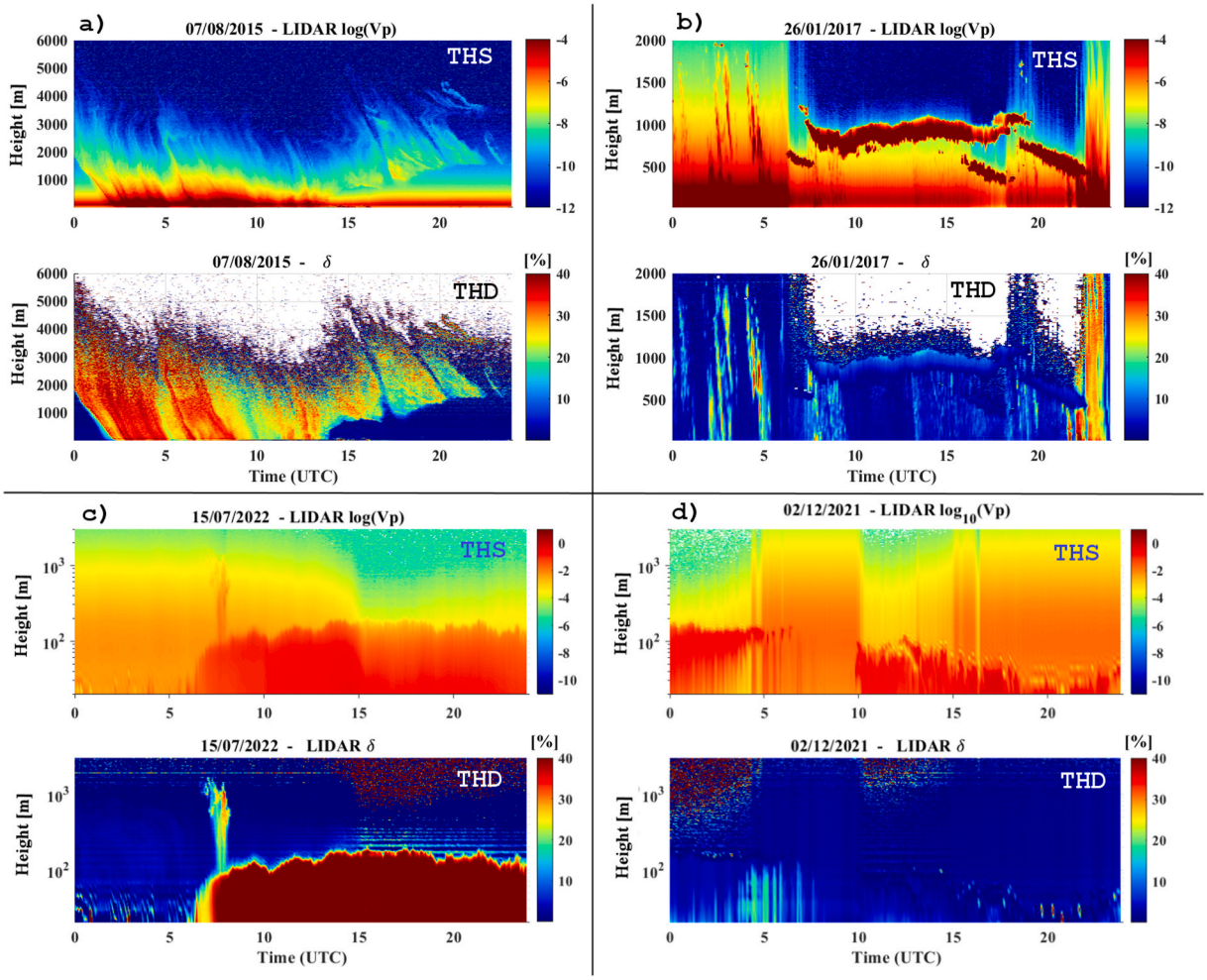

Fig. 3. Examples of THS (upper part of each subplot) and THD (lower part of each subplot) for the four PTs. a) cirrus, b) mixed phase cloud, c) ice fog, d) liquid fog. The use of logarithmic height scales improves the interpretation of 'fog'.

plot becomes noisy at a height lower than the THS plot, and THS is used instead of THD to better estimate HOF in these cases. Automating the estimation of HOF from LIDAR data in a very variable scenario like the DC atmosphere is not feasible. In cases of 'chaotic' skies, with strong fluctuations in cloud structures with time and height, the estimated HOF is marked as 'unknown'.

When derived, the HOF is used to estimate the Temperature of Formation (TOF) of precipitation from HAMSTRAD data. HAMSTRAD data was preferred to balloon sounding for estimating TOF because of the high time resolution of the HAMSTRAD measure and its reliability from the ground up to 4000 m a.g.l. It must be pointed out that the LIDAR is intended for operating up to 7000 m maximum height, but the signal from the upper heights is often noisy, so that an underestimation of HOF could occur in the case of the highest cirrus (HOF>4000 m a.g.l.). In these cases, an underestimation of HOF can occur, leading to a large error in TOF, sometimes up to ±5 °C, much greater than the error in HAMSTRAD temperature.

3. Results and discussion

3.1. Precipitation type and meteorological data

Fig. 5 shows TOF, relative humidity with respect to ice (RHice), and wind direction at HOF (from the 12:00 UTC sounding) for all the collected grains, sorted by precipitation type. In terms of temperature of occurrence, the PT classes 'ice fog' and 'cirrus' are similar and well distinct from 'liquid fog' and 'mixed phase cloud'. Since there is no supercooled water below −40 °C, the latter two classes are present at higher temperatures (Fig. 5a). The RHice from radiosounding data at HOF highlight that 'Liquid fog' and 'mixed phase clouds' occurred at higher RHice levels compared with 'ice fog' and 'cirrus'. However, this result should be considered with caution due to the several sources of uncertainties, such as the humidity sensor time-lag, the radiation error of the air temperature measurement, and data smoothing, that affects the Vaisala RS41 sensor humidity sensor at low temperature (Sommer et al., 2023). In terms of wind direction at HOF, 'cirrus' were often observed with winds from NW and NE, while all the other classes (Fig. 5c) are prevalently observed with winds from S-SE, the dominant wind direction at the surface (Argentini et al., 2014; Genthon et al., 2021).

Dominant winds, which blow from the inner regions of the continent, are low-intensity drainage flows blowing from the highest plateau south of Dome C. In the absence of maritime air intrusion (with winds from the northern quadrants), winds from the 180°–210° sector prevail. The surface wind direction is scarcely influenced by the large-scale motions because of the decoupling due to the strong ground-based temperature inversion. Heavier precipitation is thus expected from high clouds forming in air masses of coastal origin. Even if ICECAMERA is not suitable for quantitatively measuring precipitation, the wind rose of the number of ice grains per ICECAMERA scan (NPS, not shown) confirms that heavier precipitation is observed from cirrus associated with NW and NE winds of maritime origin, with twice the NPS from northern

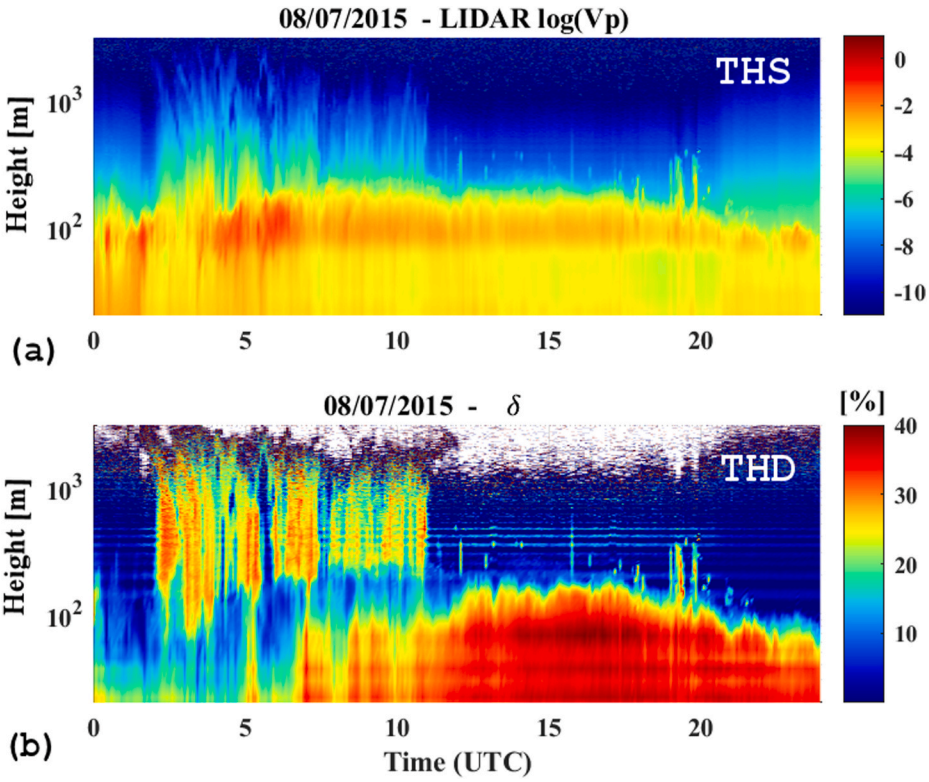

Fig. 4. An example of an ambiguous case: before 12 UTC, precipitation originating from a cirrus (above 1000 m height) falls through a low layer (≈100 m height), showing a strong signal (a) and low depolarization (b). In cases like this, no decision is taken regarding the origin of precipitation.

Table 1
The statistics of occurrence of the various precipitation types (PT) over the entire period January 2014–December 2021. For each PT, the numbers of properly classified grains are reported in both absolute and relative terms.

PT	Number of scans	% of scans	Number of grains	% of grains
Ice fog	1161	41 %	585260	34 %
Liquid fog	111	4 %	61728	3 %
Mixed phase cloud	117	4 %	57782	3 %
Cirrus	677	24 %	708175	39 %
Ambiguous case	785	27 %	382842	21 %
Total	2851		1795787	

quadrants then from the southern ones.

3.2. The height of formation of the different ice habits

The HOF for the ten selected ice habits is shown in Fig. 6. In all the boxplots of this paper the median is the middle line of the box, and the 25th and 75th percentiles are the lower and upper box edges. The lower and upper whiskers mark one interquartile below the 25th percentile and one interquartile above the 75th percentile. Above approximately 1000 m of HOF, the most common grain types resulted to be rosettes, columns, bullets, and irregular plates. Needles, irregular grains, spheroidal particles and plates resulted instead more common below 1000 m.

3.3. Ice habit and wind

The wind at HOF was derived from the local 12:00 UTC daily balloon sounding (Fig. 7). Some differences are observed between the ice habits typically observed near the ground (needles, spheroidal, irregular grains, hex plates, associated with the southerlies dominating surface winds) and the ice habits originating in clouds (bullets, columns, rosettes, compact columns). The latest habits often occurred with NW or NE winds, blowing from coastal areas. As shown by the analysis of air trajectories and precipitation models, these winds bring humid air over DC from the western Pacific and eastern Indian oceans, and are responsible for most of the snow deposition at DC (Scarchilli et al., 2011; Turner et al., 2019).

From our analysis, the HOF of precipitation associated with NW-NE winds resulted almost normally distributed around HOF = 2330 ± 1130 m (one standard deviation). According to our data, this height range was the primary source of DC precipitation.

The same statistics as Fig. 7, but in terms of surface wind direction, did not show any significant feature, with all habits apparently associated with southern surface winds. This result was expected because of the decoupling between surface winds and upper winds caused by the strong ground-based temperature inversion. A slight difference exists between ice habits of typical high height origin (bullets, columns, rosettes, irregular plates and compact columns), that resulted associated with SE surface winds, and the other ice habits of low height origin, associated with S winds.

The relationship between ice habits and surface wind speed showed no relevant features, except for an increased presence of spheroidal particles with strong surface winds (between 4 and 8 m/s), indicating that some of these particles are actually blowing snow grains. Walden et al. (2003), in the South Pole (SP) Station, found a wind speed threshold of 4 m/s for the formation of blowing snow, in summer. Another explanation for the presence of spheroidal particles with 'strong' winds is the formation of 'dots' of frost on the ICECAMERA glass. The size distribution of ICECAMERA 'spheroidals' resulted bimodal, with a second peak with median size of D ≈ 600 μm: the second peak was caused by poor segmentation of spheroidal particles when they were present in small 'dots' close together, especially in conditions of elevated RHice and strong winds. In these cases, a correct CNN classification of the particle into 'spheroidal' is done, but the feret size results are incorrect. No correlation was found between size of the spheroids

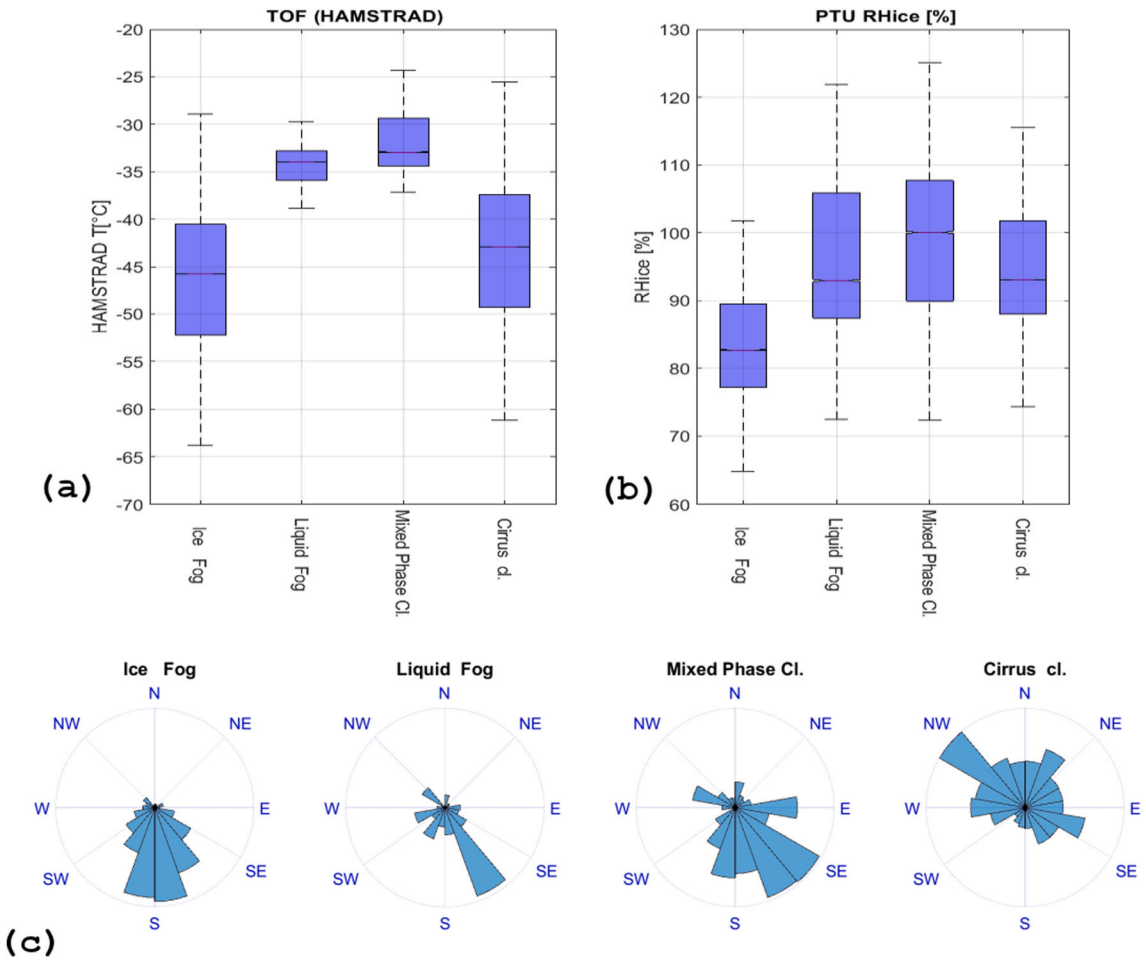

Fig. 5. Statistics of a) TOF, b) RHice, and c) wind direction at HOF for the four precipitation types.

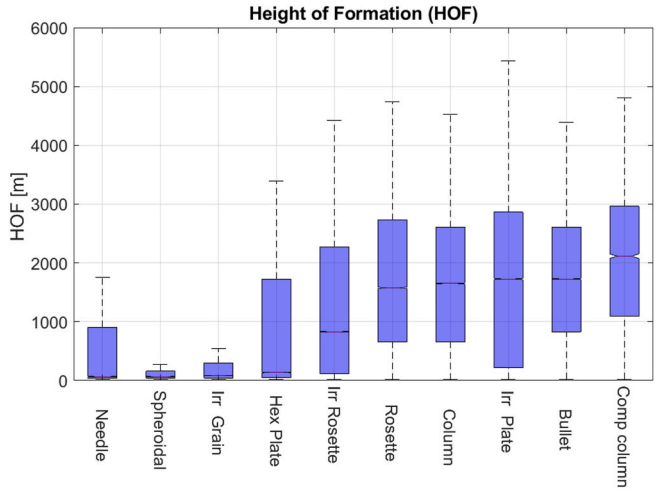

Fig. 6. The statistics of ice habit with height (HOF).

and surface wind speed in the entire range 0–15 m/s, a fact that reduces the possibility that the large detected spheroids being the result of blowing snow. In the statistical analysis we excluded 'spheroids' larger than 500 μm for these reasons.

3.4. Ice habit and size

Fig. 8 provides an overview of particle size D. The minimum detected D is 60 μm, as determined by the ICECAMERA overall sensitivity. Rosettes and irregular rosettes had a median size of around 600 μm and 400 μm, respectively. Bullets and columns in our work had a median D of about 400 and 500 μm. Compact columns, which are smaller and less common, had a median size of 250 μm. Plates showed a median diameter between 140 μm (pristine) and 230 μm (irregular). The needles were typically small, with a median length of 175 μm. This statistic includes all ice crystals observed, including DD and precipitation from clouds. DD and cloud snow may have a different mean size of an ice habit. For this reason, the comparison between our sizes and the results of other works will be better discussed in Sec. 3.5.

In Fig. 9, the size distributions of different ice habits are shown in detail. The distributions were fitted with lognormal distributions:

$$n(D) = \frac{e^{-\frac{(\ln(D) - \ln(\rho))^2}{2\sigma^2}}}{D\sigma\sqrt{2\pi}} \quad ([\mathrm{D}] = \mu\mathrm{m}) \tag{2}$$

and gamma distributions:

$$n(D) = No\, D^{\mu} e^{-\Lambda D} \quad \left([\mathrm{D}] = \mathrm{cm}, [\Lambda] = \mathrm{cm}^{-1}, [\mathrm{No}] = \mathrm{cm}^{-4}\right) \tag{3}$$

CGS units for the gamma distribution were chosen to simplify comparisons with radar literature. The goodness of each fit was estimated by calculating the Mean Squared Error (MSE) between the (normalized) fitting function and the (normalized) histogram. The gamma distribution fits better than the lognormal one for rosettes, irregular plates and columns (Table 2), while the lognormal fit outperforms it for the other habits (lognormal parameters also have the benefit of a more direct interpretation). Irregular and spheroidal particles show the worst fit,

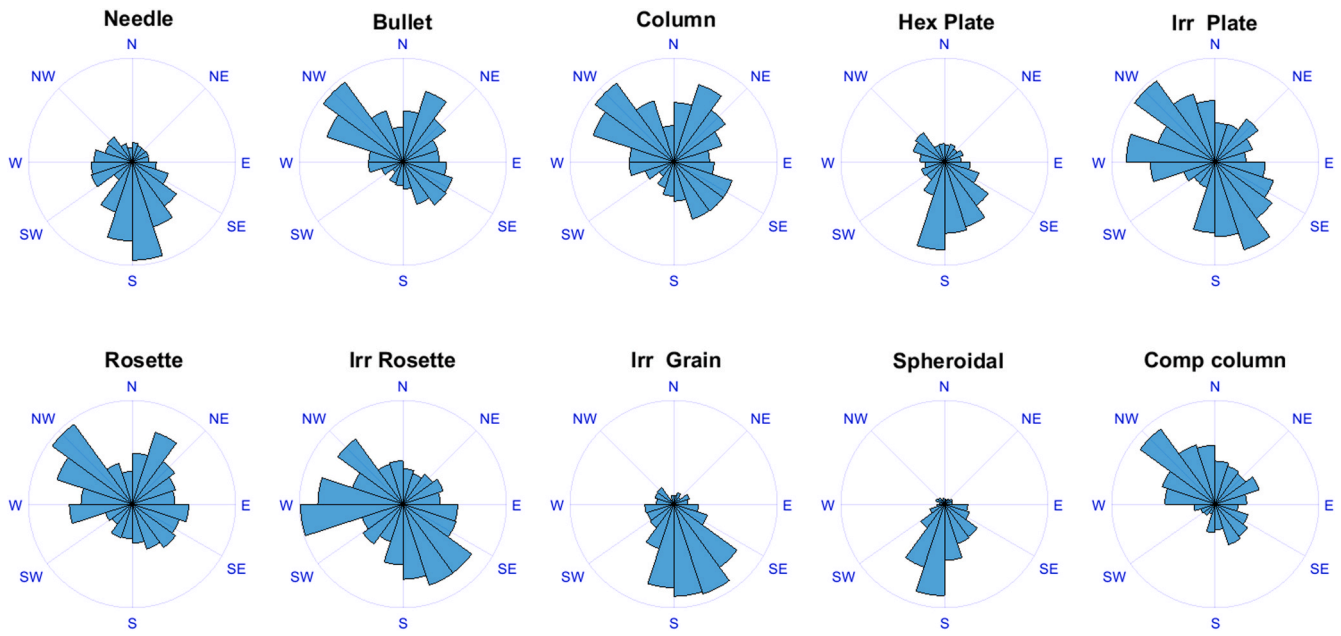

Fig. 7. Statistics of wind direction at HOF for the different habits.

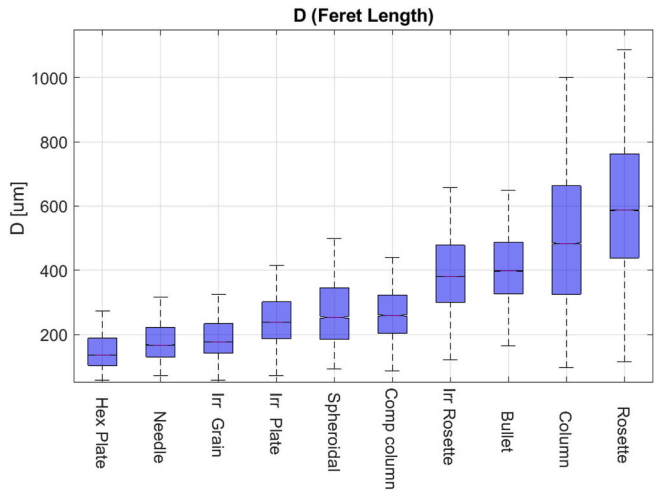

Fig. 8. Statistics of size D for the different ice habits.

certainly due to the arbitrary exclusion of the largest particles of the latter type from the statistics. The parameters of the fit functions are listed in Table 3.

3.4.1. *Ice habit and Radar reflectivity*

The radar reflectivity Z for each ice habit can be estimated on the base of the Λ values of the gamma distribution. We followed the results of Matrosov and Heymsfield (2017) for the CRYSTAL-FACE dataset. The size D of the present study is a quantity equivalent to the 'major particle dimension' used by Matrosov and Heymsfield (2017).

Z was estimated for Ka (wavelength $\lambda = 1$ cm) and W ($\lambda = 3$ mm) radars. The relationship between γ and Z was assumed to be:

$$Z = \sqrt[d]{\frac{\Lambda}{c}} \tag{4}$$

with: c = 48.1, d = −0.4 (Ka-band) and c = 32.9, d = −0.42 (W-band) (Matrosov and Heymsfield, 2017).

This relationship was assumed as a guideline even though it could be temperature and shape-dependent. Results (Fig. 10) show that most of the particle habits (with the exception of columns and pristine rosettes) are expected to produce Z < −20 dB in the W band and below −17 dB in the Ka band. Only columns and pristine rosettes have Λ <100 and thus have Z > −15 dB. Ka-band radar returns from DC precipitation are expected to be dominated by just these two ice habits. Pristine rosettes and columns represent less than 30% of all ICECAMERA particles in number: even if their relative contribution to mass, and thus to IWC, is certainly bigger, the use of Radars with a sensitivity of −15 dB would result in a dramatic underestimation of precipitation in DC. Radars with sensitivity higher than -5dB (such as MRR) would result (almost) useless. By using W-band radars like CLOUDSAT, which has as-28 dB sensitivity, all the ice habits of this study can be instead fully captured.

3.5. *Particle size and height of formation*

Size data (D) for the different ice habits were binned into logarithmic height bins and averaged. Fig. 11 shows the trend of the mean size with HOF. Many habits (e.g. rosettes) show a bimodal plot, with a small peak below approximately 100 m and a more marked peak above 100 m. The lowest peaks are supposed to be fog particles growing in supersaturated air inside the inversion layer near the surface. Ice precipitation growth processes similar to those of mid-latitude clouds take place above approximately 100 m, where a positive trend of size with HOF was found for several ice habits. Table 3 shows the coefficients of the fit regression lines defined as:

$$D[\mu m] = a^{*}\log_{10}(HOF) + b \ (HOF>80 \ m) \tag{5}$$

The correlation coefficient r is as also shown. r > 0.85 was obtained for several habits. The increase of D with HOF is more relevant for columns, rosettes (either pristine and irregular) and bullets than for the other habits. The mean size increases from 380 μm at 100 m to 600 μm at 5000 m for columns, and from 440 μm to 700 μm for rosettes.

We analyzed the increase in size with HOF for the ice habits typical of cirrus in terms of growth during fall. Crystals are supposed to grow at a constant rate as they fall. We estimated the growth rate (G = dD/dt) of the particles during their descent, assuming a constant fall speed (W = dH/dt) for each ice habit. Working experimentally in Kiruna (Sweden), Vázquez-Martín et al. (2021) measured the terminal fall speed W of ice grains for 200 μm < D < 2000 μm. We used the average W values they obtained for each habit in our work. The growth rate G is derived from

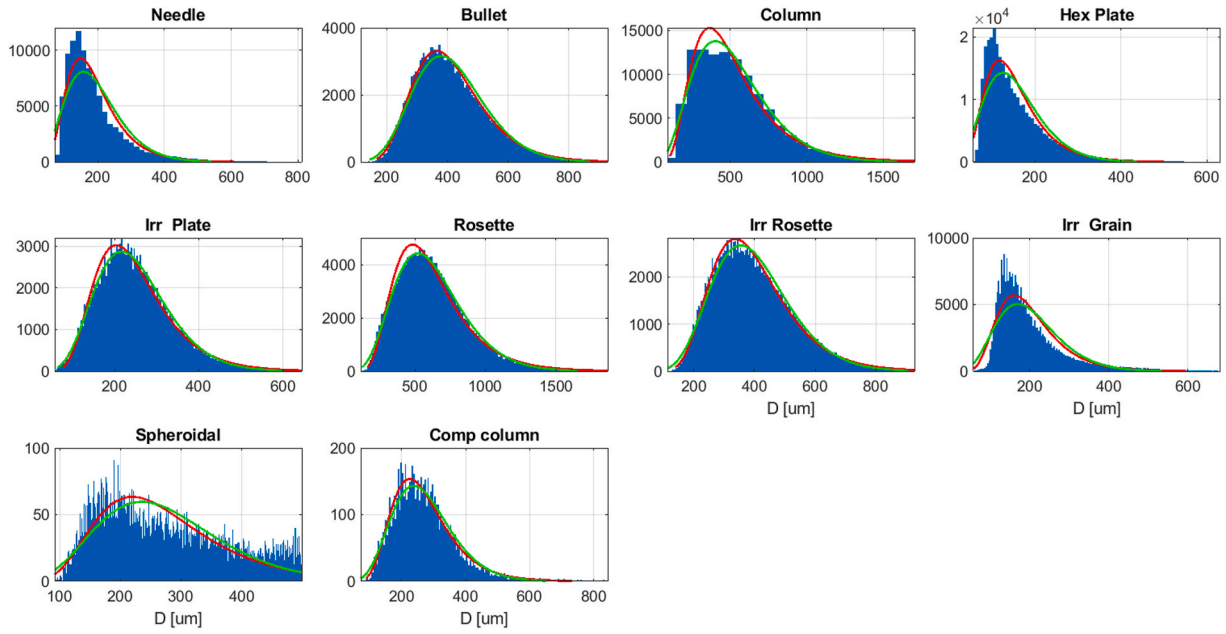

Fig. 9. Size distribution (D) for the different ice habits. Green = gamma fit; red = lognormal fit. (For interpretation of the references to color in this figure legend, the reader is referred to the Web version of this article.)

Table 2
The parameters of the gamma (green) and lognormal (red) fits for the size distributions of Fig. 9. MSE errors are also shown.

	Gamma distribution			Lognormal distribution		
Ice habit	**μ [ ]**	**Λ [cm^{-1}]**	**MSE**	**ρ [μm]**	**σ [ ]**	**MSE**
Needles	**4.3**	**277**	**3.3E-5**	**175**	**1.5**	**1.9E-5**
Bullet	**10.8**	**286**	**5.4E-6**	**396**	**1.3**	**1.4E-6**
Column	**3.3**	**84**	**7.3E-7**	**463**	**1.6**	**8.4E-7**
Hex plate	**4.2**	**340**	**8.9E-5**	**140**	**1.5**	**5.5E-5**
Irr plate	**6.8**	**316**	**4.8E-6**	**232**	**1.4**	**6.6E-6**
Rosette	**5.1**	**98**	**2.7E-7**	**572**	**1.5**	**6.6E-7**
Irr rosette	**8.2**	**233**	**4E-6**	**376**	**1.3**	**2.5E-6**
Irr grain	**5.2**	**307**	**1.9E-4**	**186**	**1.4**	**1.2E-4**
Spheroidal	**5.9**	**251**	**4.9E-4**	**255**	**1.4**	**5E-4**
Compact column	**7**	**297**	**2.9E-5**	**254**	**1.4**	**1.8E-5**

eq. (5) as:

$$G = dD/dt = W^{*}dD/dH = 0.43 * W * a * H^{-1} \quad (6)$$

Results (Table 3) show growth rates between 0.04 and 0.09 μm/s for columns and rosettes (the result G = 0.02 for bullets will be discussed a part). Bailey and Hallett (2012) studied the growth rate of ice particles at low temperatures and different ice supersaturation (σ) and temperatures (T). For the temperature range $-70\,^{\circ}C < T < -40^{\circ}C$ they found $0.002 < G < 0.02$ μm/s for $\sigma = 0.05$ (weak supersaturation), and $0.05 < G < 0.1$ μm/s for $\sigma = 0.25$ (the critical supersaturation for the nucleation of bullet rosettes below $-40\,^{\circ}C$ from Bailey and Hallett (2012)). In the case of rosettes and columns, the estimated G is compatible with the critical supersaturation ($\sigma = 0.25$) for rosette nucleation. This would mean that DC is inside the active, growing precipitation trail when the ice cloud precipitation reaches the ground.

Um et al. (2015) report crystal sizes measured inside cirrus using CPI imagery. Their broad statistics show that (for the temperature range $-67^{\circ} < T < -15^{\circ}$), an average diameter of 140 μm–280 μm is observed for columns, 120–150 μm for bullets, and 90–150 μm for hex plates. Our sizes at HOF = 100 m are around 210 μm for columns, 320 μm for bullets, and 130 μm for hex plates (Fig. 11). The sizes of columns and hex plates measured at DC for HOF = 100 m are consistent with their work. Falling from 100 m, freshly formed ice crystals have not much time to grow before they touch the ground, and their measurement is thus assimilable to measuring ice crystals inside the cirrus 'core'. The larger size of particles from higher HOF is an indication of their growth during their fall: their measurement at the ground is comparable to measuring inside the cirrus precipitation trail.

Cirrus precipitation in mid-latitudes often melts or sublimates before it reaches the surface. (Along the coasts of Antarctica, snow can sublimate when falling through a katabatic wind flow (Grazioli et al., 2017a). The absence of katabatic winds makes precipitation sublimation rare in DC. At ground level we are either inside the cirrus core (for low HOF) or inside its precipitation trail (for high HOF). This makes DC a permanent

Table 3
The parameters for the fitting functions (eq. (5)) are shown, as well as their correlation coefficients (r). The fits with r > 0.85 are highlighted. Fall speeds (W) from Vázquez-Martín et al. (2021) and growth rates (G) (eq. (6)) are reported.

Ice habit	a	b	r	W [m/s]	G [μm/s]
Needle	6,6	154,1	0,51	0,34	0,006
Bullet	49,4	242,5	0,89	0,3	0,017
Column	148,6	26,6	0,88	0,3	0,045
Hex Plate	18,3	89,1	0,81	0,39	0,022
Irr Plate	21,3	175,4	0,78	0,4	0,016
Rosette	184,3	8,7	0,89	0,59	0,093
Irr Rosette	71,2	186,5	0,87	0,59	0,047
Irr Grain	30,0	112,6	0,72	0,45	0,030
Spheroidal	-11,2	463,8	0,08	0,5	-0,006
Comp column	29,5	163,5	0,60	0,41	0,021

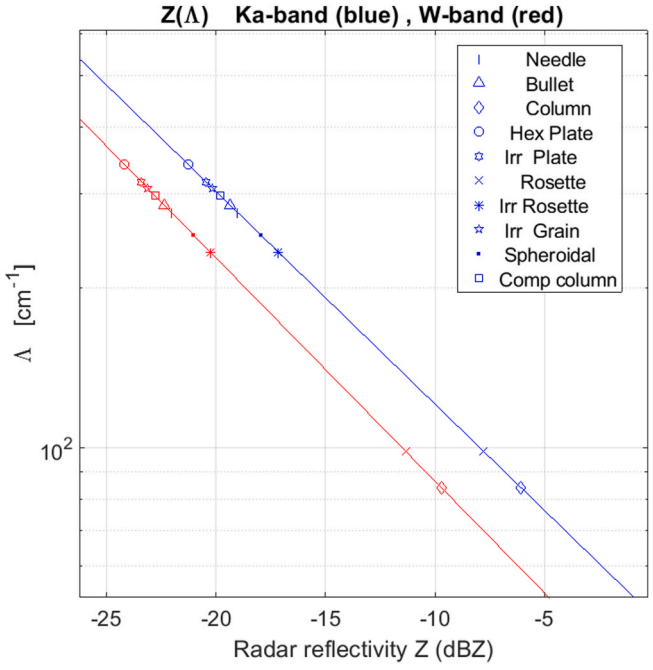

Fig. 10. Radar reflectivity Z estimated as a function of Λ (Matrosov and Heymsfield, 2017) for the size distributions obtained in this work. Red = W band; Blue = Ka band. (For interpretation of the references to color in this figure legend, the reader is referred to the Web version of this article.)

substitute for the airborne platforms used for in-situ ice cloud studies.

Bullet particles need a separate discussion. Assuming that bullets originate from the break-up of bullet rosettes, we would expect the size of rosettes to be ≈ 1.5 times larger than the size of bullets (Fridlind et al., 2016). It is expected that both habits will experience similar growth rates during their fall. According to Table 3, rosettes that originate at 2000 m height are 1.53 times bigger than bullets from the same height, as expected by Fridlind et al. (2016). Rosettes falling from 100 m height are instead only 1.1 times larger than bullets falling from the same height. Also, the growth rate for bullets (Table 3) was much lower than that of rosettes (either pristine or irregular) and columns. These discrepancies (including the difference between the size of bullets at HOF = 100 m and results of Hu et al. (2006)) indicate that either the large bullets observed at low heights in DC are not caused by break-up of falling rosettes, or that many bullets are an artefact due to a poor segmentation of ICECAMERA images of columns.

Needles, spheroids and irregular grains were mostly observed below 2000 m HOF (Fig. 6). Fig. 11 showed no correlation between their size and HOF. Above 2000 m, their observations are sporadic. When estimating HOF for precipitation from LIDAR plots, the same HOF may be attributed to particles (such as needles, which are barely visible in LIDAR plots) of much lower origin.

3.5.1. *Comparison of precipitation size with literature*

With the results of Fig. 11 we can compare our size of the different ice habits as observed in DD (low height origin) and in cloud precipitation (higher height) with the results of other direct measurements of precipitation carried out in inner Antarctica.

Regarding diamond dust, we will compare our results for HOF <100 m (Fig. 11) with available DD studies:

Columns in DD. Our results show that the size of columns from near the ground is 250 μm. Kikuchi et al. (1979) at SP found columns of D ≈ 90 μm. Smiley et al. (1980) found at SP (winter) in low height precipitation ('type IV' in their paper) columns and bullets with an average length in the range of 114–162 μm. Walden et al. (2003) at SP in winter studied DD obtaining for columns with average D = 61–85 μm. Lawson et al. (2006) found in DD columns of average D ≈ 80 μm. Our results indicate columns larger by a factor of 2–4 than in previous DD studies.

Plates in DD. Hex plates near the ground resulted to have a size of D = 125 μm. Smiley et al. (1980) found for plates an average D ≈ 110 μm. Walden et al. (2003) found for plates an average D ≈ 27 μm. Lawson et al. (2006) found in DD plates of average D ≈ 60 μm. To sum up, our findings reveal that the hex plate dimensions are ≈1.1–4 times larger than those of the previous DD studies.

Regarding precipitation from clouds, we compare our results for HOF = 2000 m (Sec. 3.3) with previous studies reporting cloud precipitation.

Columns in precipitation. Our results show a column size of D ≈ 500 μm. Satow (1983) found an average D ≈ 287 μm. Smiley et al. (1980) found ('type I,III' in the paper) D ≈ 110 μm. Walden et al. (2003) D ≈ 190–240 μm. Lawson et al. (2006) found an average D ≈ 60–110 μm. Kameda et al. (2007) worked in Dome Fuji throughout a year in conditions similar to DC. Their median size for columns (as derived by re-scanning their paper) is D ≈ 430 μm. In summary, our results show

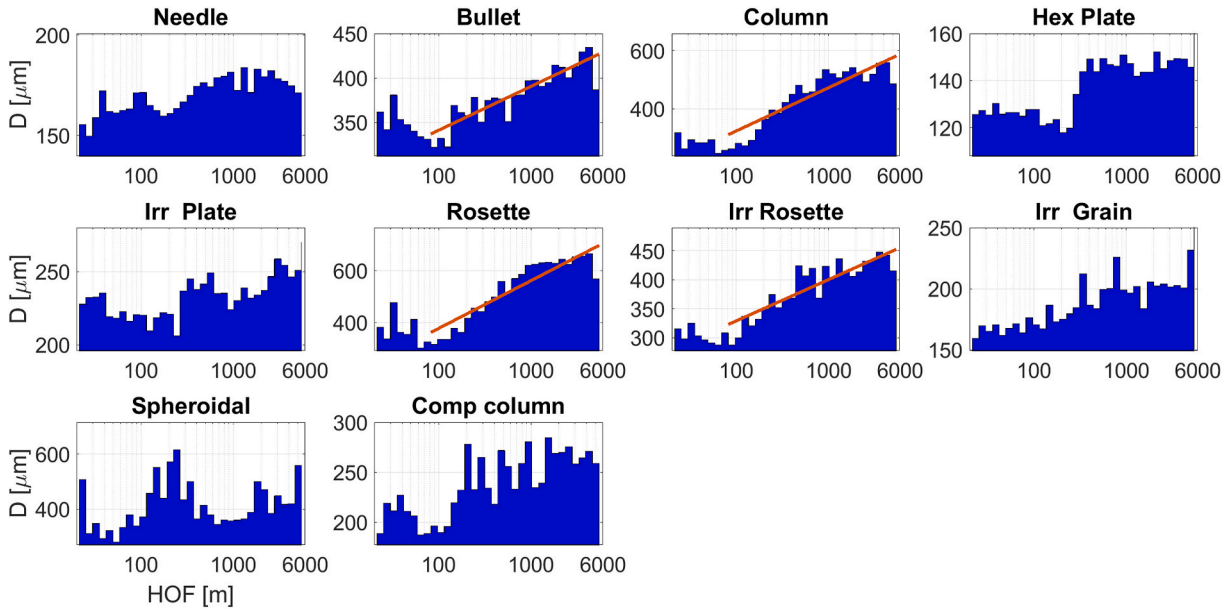

Fig. 11. The trend of size with HOF [m] for the ten ice habits. Fit lines between 100 m and 6000 m HOF (eq. (5)) are shown for cases with r > 0.85.

that columns are ≈1.1–5 times larger than previous studies.

Rosettes in precipitation. Our results show a size of D ≈ 620 μm for rosettes from clouds. Lawson et al. (2006) found an average D ≈ 100 μm. The size of Kameda et al. (2007) (as derived by re-scanning the paper) is D ≈ 500 μm. Our results show that rosettes are larger by a factor of 1.2–6 times than previous studies carried out in the inner Antarctica.

Summarizing, the plates, columns, and rosettes observed in this work are larger than those observed in most other studies carried out in inner Antarctica, which calls for a discussion. The particle size threshold in this work is D = 60 μm, and our size distributions cannot be directly compared with the results of works that include much smaller particles. The slow terminal velocity of small particles could also play a role in increasing the time scale for the ice crystals to settle to the ICECAMERA surface (Kim et al., 2014). A differential speed of sedimentation can contribute to an increase in the number of big particles deposited on the ICECAMERA surface, compared to what is observed when sampling the crystals directly in the air.

The growth of the particles on the deposition surface of ICECAMERA before measurement is ruled out, because the deposition surface is slightly warmer than the environment and thus the surface air of ICECAMERA is under-saturated. Some small particles (D < 200 μm) are instead lost in sublimation before being observed, and our size distributions could thus be shifted toward larger sizes compared with other works for the ice habits of small average size, such as plates, needle, compact columns and irregular particles. This is a certainly a problem in the warm months, but much less in winter, when sublimation on ICECAMERA is much slower. For large particles (such as rosettes and columns), these effects are negligible, and the obtained sizes can be considered certain.

Size for columns and rosettes in this work are similar to those observed by Kameda et al. (2007), who photographed precipitation deposited on glass surfaces, a technique that is subject to the same possible uncertainties as those listed for ICECAMERA, particularly in the selective sublimation of small particles. In 2022, ICECAMERA was modified in order to reduce the possible losses for sublimation. The cleaning of the deposition surface is now done using a carbon-fiber wiper, instead of heating up cyclically the glass. The effects of this change on the measurement of small ice grains are being currently investigated.

3.6. Analysis of the ice habit composition

Each ICECAMERA scan 'k' provides a normalized vector $Q_k = [P_1, \ldots. P_{10}]$ (here named 'ice habit composition'), where P_i (i = 10.10) is the relative occurrence of the ice habit 'i' in the scan 'k'. The analysis was limited to scans that contained over 100 particles.

3.6.1. Habit composition changes with the height of formation

The ice habits composition was analyzed in relation to HOF (Fig. 12 and Table 4). Close to the ground (with a thermal inversion reaching −80 °C surface temperature in winter), the relative presence of needles resulted greatest (in agreement with Bailey and Hallett (2009)). Plates and irregular grains are also prevalent in the first 200 m above ground. The habit above 100–200 m gradually shifts towards bullets, columns, rosettes (both pristine and irregular), and irregular plates.

3.6.2. The mean ice habit composition of the four precipitation types

The purpose of this section is to examine the differences in habit composition among the four precipitation types. The study was conducted to find an automated method to classify the PT based on the composition of the ice habit as derived from the visual observation of precipitation on the ground. This topic is particularly relevant for determining the origin of precipitation in high plateau sites, typically unequipped with depolarization LIDARs or other remote sensing instruments for the determination of the cloud structure.

3.6.2.1. Mean ice habit composition of the four precipitation types. The average habit composition for the four PT is summarized in Fig. 13. Ice fogs resulted characterized by hex plates, irregular grains and needles. Irregular grains, irregular rosettes and hex plates resulted common in liquid fog. Mixed phase clouds showed an average composition similar to that of liquid fogs, with a higher concentration of irregular plates and irregular rosettes, and less irregular grains. Bullets, rosettes, columns (and hex plates) resulted common in cirrus precipitation. Spheroidal particles resulted quite uncommon: even if fogs have a higher percentage of them (2%), their presence is secondary, as already observed by Gultepe et al. (2014) and Kim et al. (2014).

3.6.2.2. Detailed ice habit composition of the four precipitation types. A more detailed statistic is obtained when analyzing the ice habit composition Q_k of each ICECAMERA scan. Q_k is a 'compositional' data

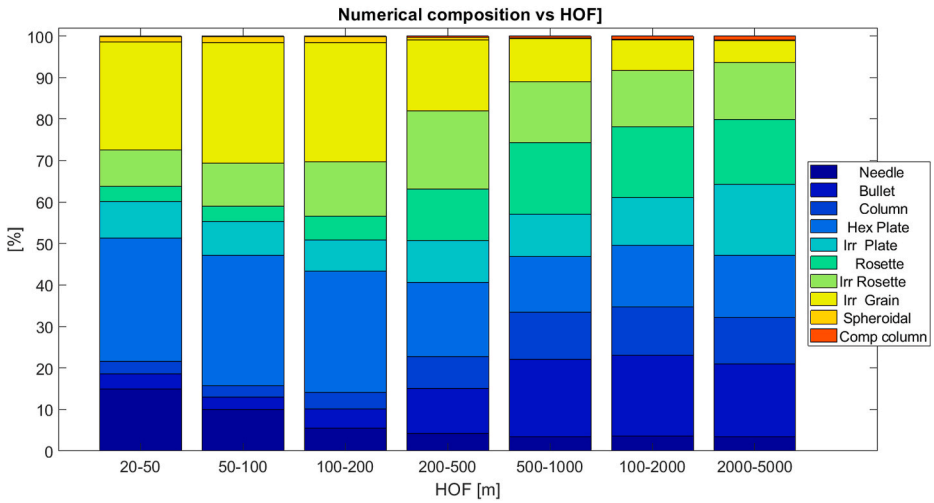

Fig. 12. The average ice habit composition as a function of HOF. Changes occurring in the lowest layers are evidenced by the logarithmic binning.

Table 4
Ice habit composition [%] versus HOF. HOF bins are logarithmic.

HOF range [m]	20–50	50–100	100–200	200–500	500–1000	100–2000	2000–5000
Needle	14,9	10	5,5	4,1	3,3	3,5	3,4
Bullet	3,6	2,9	4,5	10,8	18,7	19,4	17,4
Column	3,1	2,7	3,9	7,7	11,3	11,7	11,2
Hex Plate	29,5	31,4	29,2	17,8	13,3	14,8	15
Irr Plate	8,8	8	7,4	10	10,2	11,5	16,9
Rosette	3,6	3,7	5,6	12,4	17,2	17	15,7
Irr Rosette	8,7	10,3	13,1	18,8	14,7	13,4	13,6
Irr Grain	26	29,1	28,7	17	10,3	7,3	5,2
Spheroidal	1,2	1,3	1,3	0,5	0,1	0,1	0,1
Comp column	0,1	0,1	0,1	0,3	0,5	0,7	1

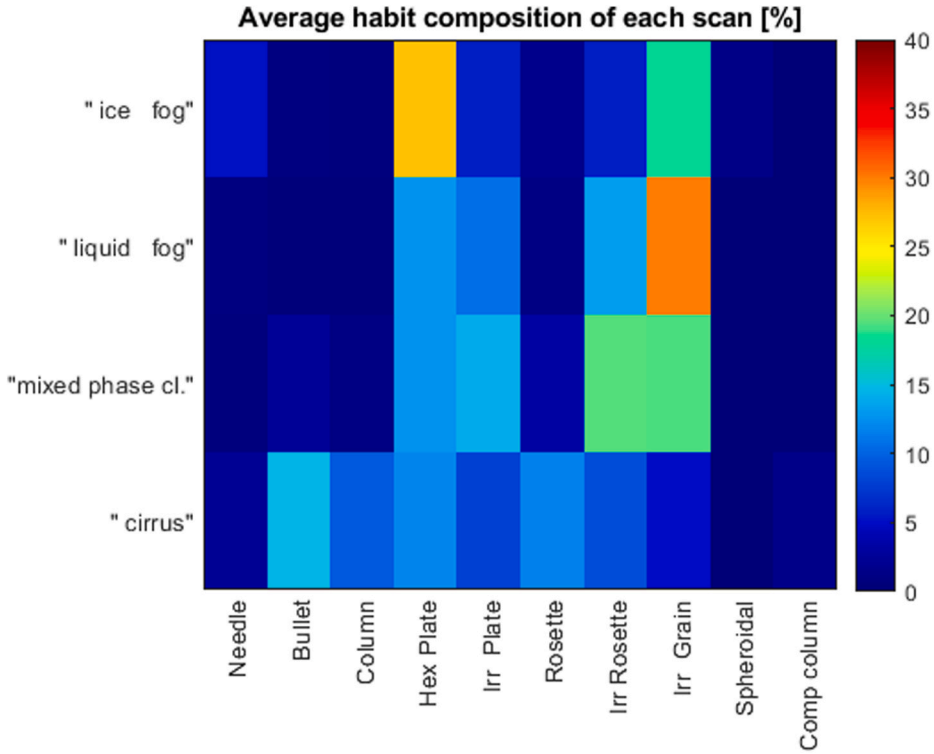

Fig. 13. The average composition of precipitation in the four PTs. False colors represent the mean habit composition (%). (For interpretation of the references to color in this figure legend, the reader is referred to the Web version of this article.)

point (having a constant sum of 1): ordinary statistical methods like multivariate analysis cannot be used directly on a compositional data set. Compositional data analysis is required for this type of data (Aitchison, 1982, 2005; Pincus and Aitchison, 1988). After a proper logarithmic coordinate conversion, the ordinary methods of multivariate analysis, such as the Canonical Discriminant Analysis (CDA, e.g. Trujillo-Ortiz et al., 2004) can be applied (Appendix B). Fig. 14 displays the results of the CDA for the first two canonical axis: each point represents the 'projection' of Qk on the sub-space of the first two canonical axis. Ellipse marks the χ^2 confidence bound ($p = 0.05$). 'Cirrus' and 'ice fog' have the best separation along the first canonical axis. The clusters for 'mixed phase clouds' and 'liquid fog' are less distinct, and weakly separated along the second canonical axis. The weak separation of these two clusters is probably also due to the relative scarcity of their data points (Table 1). The Wilk's Lambda (see Appendix B) resulted to be 0.35, with $\chi^2 = 2856$, $df = 27$, $p < 0.05$. The weak separation of the four clusters in the plane of the first two canonical variables means that the classification of the origin of precipitation into the four PTs from the analysis of the composition of precipitation is not certain at the $p = 0.05$ significance level.

For the first two canonical axis (Fig. 14) in Table 5 the centroids of the four PT clusters and the coefficients of two canonical functions are reported. The centroids of the best defined clusters 'Ice fog' and 'Cirrus', and the coefficients of the functions 'directed' toward these two centroids are marked in red and blue, respectively.

The coefficients refer to the 'orto' space (Appendix B), but having used the ALR transformation function, these coefficients are also a proxy of the importance of the different ice habits in the discrimination of the four PTs. The coefficients of the first canonical function indicate that needles, columns, hex plates, irregular rosettes, irregular grains, and spheroids define the cluster ('ice fog'), while bullets, rosettes and compact columns define the cluster ('cirrus'). 'Columns' play a role in clustering ice fog, despite the average composition of ICECAMERA scans (Fig. 13) suggesting that they are mainly associated with cirrus. Nonetheless, other linear discriminant analyses were tested by using the MATLAB Classification learner app, and all yielded the same result for 'columns'.

Table 5
Cluster coordinates along the first two canonical axis and coefficients of the two canonical function. red = 'ice fog'; blue: 'cirrus'.

	function 1	function 2
Ice Fog	-2,259466524	-1,134528432
Liquid Fog	-1,52674977	0,306720285
Mixed Phase Cl.	-0,622290707	0,149497623
Cirrus cl.	0,356438882	-1,078195573
Needle	−0,233932223	−0,180156176
Bullet	0,35182456	0,086447792
Column	-0,259835521	0,0896145
Hex Plate	-0,178716696	-1,102611638
Rosette	0,13480508	-0,269857453
Irr Rosette	-0,198136865	-0,138858563
Irr Grain	-0,427459127	0,663760512
Spheroidal	-0,198662997	0,189389278
Comp column	0,480804185	-0,017250935

Fig. 15a shows the Confusion Matrix (CM) for the CDA classification. The percentages along the bottom row ('positive predictions') show the probability for a predicted PT (output of the classifier) to be the same, true PT in the real world. The CM shows that an overall 72% precision of PT classification is expected when applying the CDA clustering to the ice

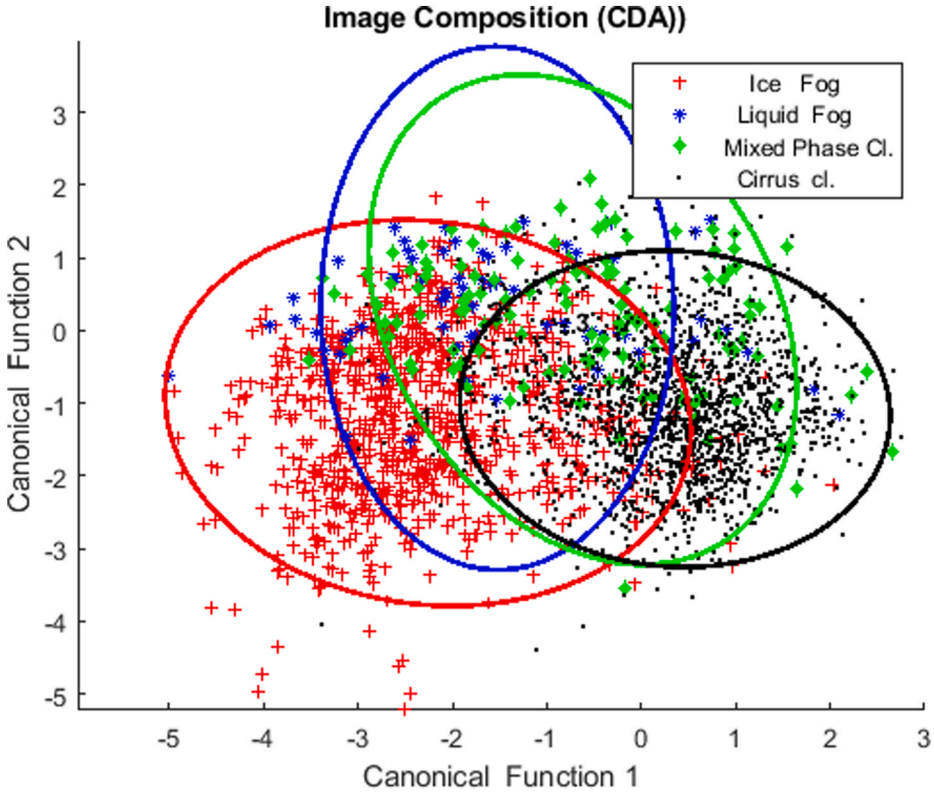

Fig. 14. The four PT clusters on the first two canonical axis. $p = 0.05$ is the confidence level marked by the ellipses. Different colors mark data and confidence ellipses for the four PTs. (For interpretation of the references to color in this figure legend, the reader is referred to the Web version of this article.)

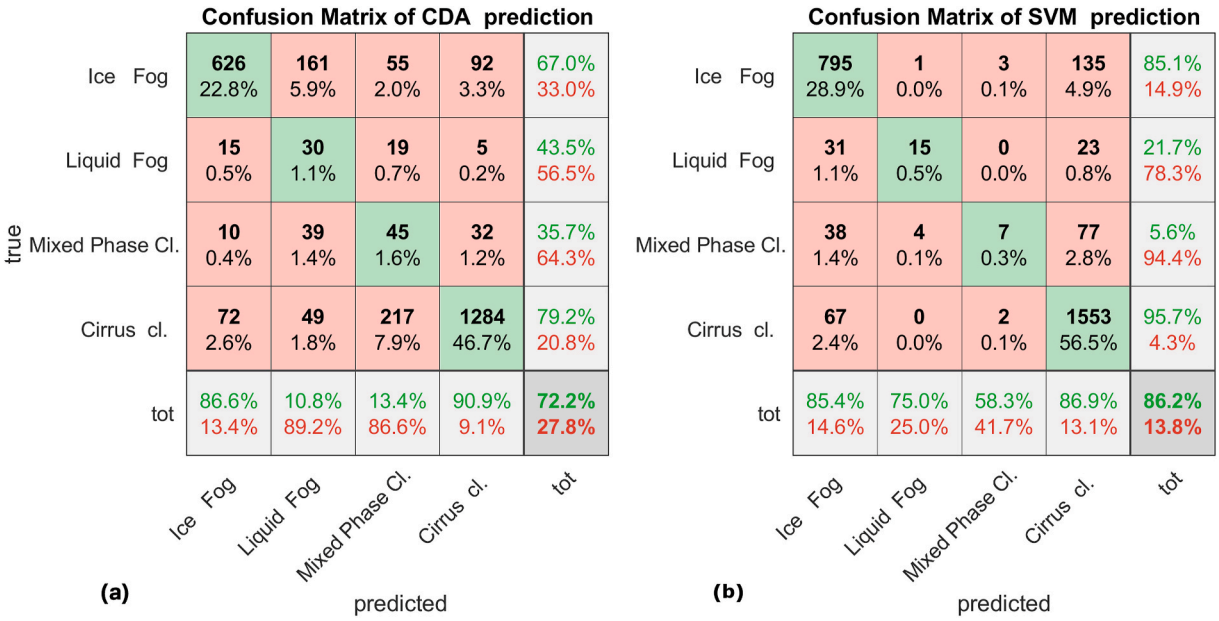

Fig. 15. Confusion Matrices for: a) CDA classifier, b) SVM classifier.

habit composition. A quite good positive prediction is expected for 'ice fog' (87%) and 'cirrus' (91%). The low accuracy of the prediction of the other PTs is probably due to their limited representativeness in the dataset. 'Liquid fog' is often mistaken by CDA for 'ice fog' or 'mixed phase cloud', and only 11% of classifications for this type of precipitation are accurate. 'Mixed phase clouds' are often misclassified as 'cirrus' or 'ice fog'.

A quadratic Support-Vector Machine (SVM) (Cortes, 1995) classifier was created to perform the same task as CDA, still into the 'orto' space, but in a machine-oriented manner. This algorithm was chosen after evaluating the various algorithms offered by the MATLAB 'Classification Learner App'. There are some differences between the CM of SVM (Fig. 15b) and the CM of CDA: the positive prediction for 'liquid fog' and 'mixed phase cloud' resulted above 58% for both classes, while the prediction for ice fog and cirrus is almost unchanged. As a consequence, the quadratic SVM classifier outperforms CDA in the identification of the correct PT in the case of 'liquid fog' and 'mixed phase clouds'.

Observing that the mean size of various ice habits changes with HOF (Fig. 11), a test was conducted for improving the determination of PT from the observation of precipitation. We considered the possibility of a better separation of the PT clusters of Fig. 14 by including in the multivariate analysis also the size Dk of the different ice habits 'k', as measured (and averaged) in each ICECAMERA scan. We thus analyzed the compositional space of vectors [Qk, Dk]. In order to avoid singularities in the ALR, the unavailable median sizes (caused by the absence of some ice habit in the scan) were replaced with the sizes averages across the entire dataset. The accuracy of the CDA prediction was not improved by the inclusion of mean sizes in the CDA analysis (Fig. 16a). The Wilk's test (Wilk = 0.33, χ^2 = 3031, df = 57) do not significant improvements. The quadratic SVM model showed some improvement

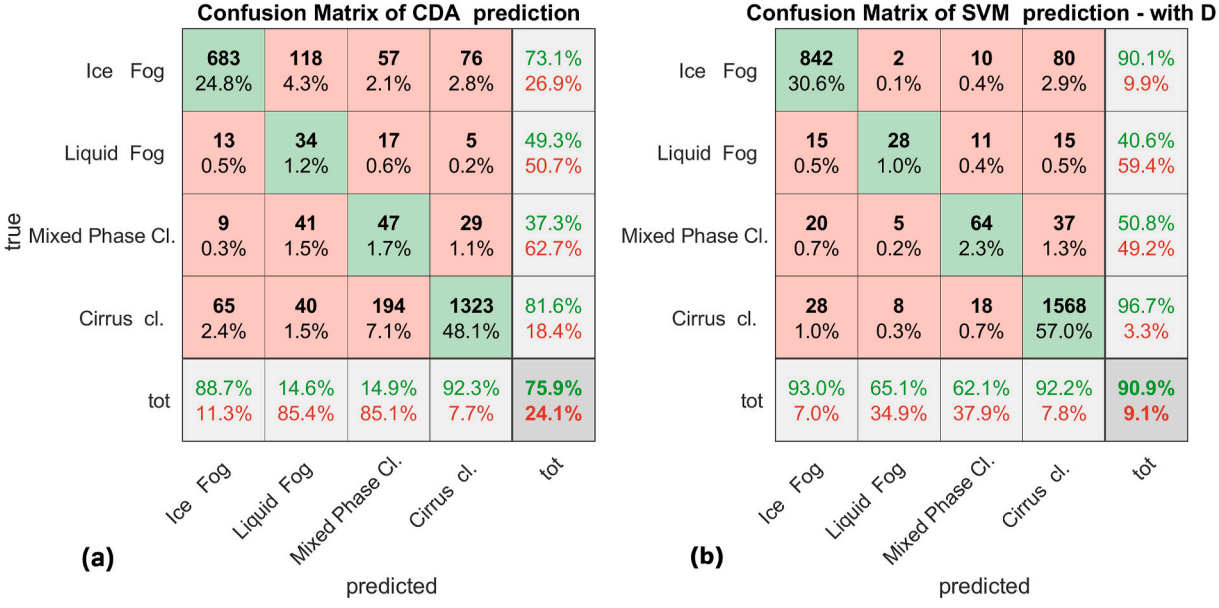

Fig. 16. Confusion matrices (including mean sizes Dk in the data set). a) CDA classifier, b) SVM classifier. In this model, higher positive prediction rates (above 92% for 'ice fog' and 'cirrus') were obtained than those of Fig. 15.

(Fig. 16b), with positive prediction rates increasing over 92% for 'ice fog' and 'cirrus'. To achieve the slight improvement in PT classification rates, a significant effort must be put into measuring the mean size of each ice habit. A task difficult to accomplish in DC, especially in the cold polar winter.

4. Conclusions

The combined use of ICECAMERA, depolarization LIDAR, HAMSTRAD, meteo data and radiosondes over almost a decade (2014–2021) resulted into a unique data-set of precipitation for inner Antarctica. The work provided direct observation of ice precipitation, which is rare on the high plateau. The size and habit of ice grains of size $D > 60$ μm were obtained from in-situ observation with the help of machine-learning, while the height and temperature of origin were obtained from remote-sensing techniques. The type of layer originating precipitation was deduced from LIDAR false color plots, and classified into four types: 'ice fog', 'liquid fog', 'mixed phase cloud', and 'cirrus'.

Observed precipitation cases were primarily sourced by 'cirrus' and 'ice fog' (e.g. Fig. 16), while 'liquid fog' and 'mixed phase clouds' were less common.

Statistics were obtained for the height of formation, temperature, and wind direction at the height of formation for ten ice habits typically observed in DC. Needles, hex plates, spheroidals and irregular grains prevailed in precipitation from low heights, associated with winds from the South. Rosettes, bullets, columns, and irregular plates were associated with cirrus clouds and NW-NE height winds blowing from coastal areas. Winds from the NW and NE, which originated in coastal areas and blow at heights between 1200 and 3500 m, contributed to the majority of the observed precipitation.

For columns, rosettes and bullets, (typically associated with 'cirrus'), we observed a marked increase in size with the height of origin. This effect can be attributed to the growth of ice particles while descending in ice-superasaturated air at a rate of 0.02–0.09 μm/s.

Rosettes, columns, and plates in DD or cloud precipitation were found to be larger in this study than in most other inner Antarctic studies.

Simulations of radar reflectivity Z demonstrated that W-band radars (with a sensitivity better than −25 dB, like CLOUDSAT), can capture all the ten ice habits in DC. K-band radars with a sensitivity of -5dB, are only able to detect a few precipitation events that are dominated by large pristine rosettes/columns.

In the precipitation originating within the first 200 m above ground, ice habit composition was dominated by needles, hex plates and irregular grains. Precipitation from higher heights resulted dominated by bullets, columns, rosettes (either pristine and irregular), and irregular plates.

An attempt to identify the type of layer originating precipitation from the ice habit composition of precipitation was carried out by means of compositional analysis followed by CDA and SVM classifiers. The quadratic SVM technique allowed for an accuracy of better than 85% in classifying 'ice fog' and 'cirrus' precipitation, with a lower accuracy for 'liquid fog' (75%), and 'mixed phase clouds' (58%). The inclusion of the habit-resolved measurements of size in the analysis improved only slightly the accuracy of the classifiers.

5. Limitation of the analysis

The analysis above has several limitations.

1) The lower size limit of ICECAMERA misses ice grains smaller than 60 μm, and small grains can also be missed for sublimation, especially during summer.
2) The results may not be representative of all precipitation because the ICECAMERA data set, although covering almost a decade, is not continuous. Dome C's harsh conditions make it hard to operate a similar instrument consistently. In cases of intense precipitation, separating ICECAMERA scans into isolated crystals is not feasible, so the data set excludes such cases.
3) Filtering out bad LIDAR data and ambiguous LIDAR cases where the layer of origin of precipitation is unclear reduces the data set for analysis of the precipitation origin.
4) With the exception of temperature (derived from HAMSTRAD), the other meteorological quantities at HOF rely on daily 12:00 UTC radiosondes. Even if RS humidity and wind direction were used in a minor way in this work, it still limits the analysis's validity.

Code and data availability

The CNN training images are available in Zenodo (Del Guasta, 2022b). The canonical and SVM models discussed in this work can be found in Zenodo (Del Guasta and Ricaud, 2023). The models and data are coded using Matrosov and Heymsfield, 2017. All the LIDAR plots, HAMSTRAD data, and ICECAMERA scans utilized in this paper can be found in the same Zenodo repository (Del Guasta and Ricaud, 2023).

CRediT authorship contribution statement

Massimo Del Guasta: Writing – review & editing, Writing – original draft, Visualization, Validation, Resources, Project administration, Data curation, Conceptualization. **Philippe Ricaud:** Resources, Methodology, Investigation, Funding acquisition, Formal analysis, Data curation, Conceptualization. **Claudio Scarchilli:** Methodology, Investigation, Formal analysis, Data curation, Conceptualization. **Giuliano Dreossi:** Investigation, Funding acquisition, Formal analysis, Conceptualization.

Declaration of competing interest

The authors declare that they have no known competing financial interests or personal relationships that could have appeared to influence the work reported in this paper.

Acknowledgements

We are thankful for the Italian Antarctic Project "Progetto Nazionale Ricerche in Antartide" (PNRA) that supported this work with the projects PNRA 2009/A4.1 (ICECAMERA), PNRA 2013/AC3.05 (PRE-REC), PNRA16_00189 (FIRCLOUDS), PNRA18_0058 (ICE-OPT), PNRA18_00031 (WHETSTONE). We are grateful for the local meteorological data and PTU soundings that were provided by the 'Osservatorio Meteo-Climatologico Antartico' (PNRA 14_00100). The HAMSTRAD programme was funded by the Institut National des Sciences de l'Univers (INSU)/Centre National de la Recherche Scientifique (CNRS), the Institut polaire français Paul-Emile Victor (IPEV), Météo-France and the Centre National d'Etudes Spatiales (CNES). We are grateful to the logistics staff and winter-over crews at Concordia station: only their hard work in a such harsh environment allowed us to conduct our scientific activities. We want to express our gratitude to the winter-over people who have specifically attended LIDAR and ICECAMERA over the years: Xavier Joffrin, Giampietro Casasanta, Vito Stanzione, Laura Caiazzo, Moreno Baricevic, Meganne Christian, Wenceslas Marie Sainte, Rodolfo Canestrari, Angelo Galeandro, Alessia Nicosia.

APPENDIX A. LIDAR technical details

Laser: Quantel Brio ($\lambda = 532$, linear polarization). A $\lambda/2$ plate is used in order to align the laser polarization with the analyzed parallel polarization. Laser power is dynamically modulated to keep the receiver system unsaturated at all ranges.

Telescope: refractive, lens diameter 100 mm. Focal length 300 mm.

Field of view (FOV): 1.2 mrad full angle. (Determined by the interference filter acceptance angle).

Interference filter: Andover 001FC10-532, $\lambda o = 532$ nm, peak transmittance To = 59%, BW = 0.14 nm @ 50% transmission, thermally stabilized 30 °C ± 0.5 °C.

Data acquisition: Licel GmbH, analog, 2 channels (532 nm p, s). Vertical resolution: 7.5 m.

Averaging: 500 shots/measurement Time resolution of the measurement: 5 min.

Height range: 10 m ≈ 4000 m (depolarization), 50 m ≈ 7000 m (signal).

APPENDIX B. Compositional data analysis

The analysis of compositional data with multivariate methods implies the transformation of the original compositional data space ('simplex', in statistical jargon), of dimension J into another data space ('orto'in statistical jargon) of dimension J-1 by means of a transformation function that replaces the compositional dataset with a set of logratios. Once the transformation is performed, analysis, visualization and inference carries on as before, but always taking into account the interpretation in terms of logratios. In Aitchison, (1982) earliest work, the Additive Logratio Transformation (ALR) was proposed, where one component is chosen as the denominator, or reference, with all the other components as numerators. Thus, if there are J components in the 'simplex', with values P1, P2, …, PJ, there are J−1 logratios in the ALR set with respect to the selected reference component (denoted by Pref), of the form:

$$\mathrm{ALR}(j|\mathrm{ref}) = \log(Pj/Pref),\ j = 1,\ \ldots,J,\ j \neq \mathrm{ref} \tag{6}$$

A variety of logratio transformations have been proposed since then, with better mathematical properties (isometry), but with complex interpretations. It is shown in a variety of contexts (e.g. Greenacre, 2018) that a set of simple ALR logratios comes sufficiently close to being isometric for practical purposes. A small loss of isometry is traded off in favor of the benefit of a simpler and clearer interpretation of the logratio variables.

In this work, the reference variable used in ALR was the ice habit 'irregular plates', which is present in all four precipitation classes with a relatively flat percentage. We also tested the use of 'irregular grains' as a reference variable, resulting in very similar results. In order to avoid singularities in ALR due to the total absence of some ice habits into some ICECAMERA scans, the CNN probabilities of classification for each ice grain ($Pcnn_i$, $i \in [1, 10]$) were used in this analysis for calculating Q_k, instead of the simple presence-absence of the class 'i'.

After ALR transformation, it is possible to perform multivariate analysis. Canonical Discriminant Analysis (CDA) was used to analyze the clusters in the orto space. CDA derives the canonical coefficients parallels that of one-way MANOVA, and it finds linear combinations of the quantitative variables that provide maximal separation between the classes or groups. The canonical coefficients are then rotated back into the 'orto' space. In order to measure how the different precipitation classes are separated by CDA, Wilks' lambda test was used: a value near zero indicates a good separation between groups, while a value near one indicates no separation between groups. The Bartlett's approximate chi-squared statistic was used to test the Wilk's value.

References

Aitchison, J., 2005. A concise guide to compositional data analysis. https://imae.udg.edu/Activitats/CoDaWork05/A_concise_guide_to_compositional_data_analysis.pdf. (Accessed 15 November 2023).

Aitchison, J., 1982. The statistical analysis of compositional data. J. Roy. Stat. Soc. B 44 (2), 139–177. http://www.jstor.org/stable/2345821. (Accessed 15 November 2023).

Aristidi, E., 2005. An analysis of temperatures and wind speeds above Dome C, Antarctica. Astron. Astrophys. 430, 739–746. https://doi.org/10.1051/0004-6361:20041876.

Argentini, S., Pietroni, I., Mastrantonio, G., Viola, A.P., Dargaud, G., Petenko, I., 2014. Observations of near surface wind speed, temperature and radiative budget at Dome C, Antarctic Plateau during 2005. Antarct. Sci. 26, 104–112. https://doi.org/10.1017/s0954102013000382.

Austin, R.T., Heymsfield, A.J., Stephens, G.L., 2009. Retrieval of ice cloud microphysical parameters using the CloudSat millimeter-wave radar and temperature. J. Geophys. Res. 114, D00A23 https://doi.org/10.1029/2008JD010049.

Avery, M., Winker, D., Heymsfield, A., Vaughan, M., Young, S., Hu, Y., Trepte, C., 2012. Cloud ice water content retrieved from the CALIOP space-based LIDAR. Geophys. Res. Lett. 39, L05808 https://doi.org/10.1029/2011GL050545.

Bailey, M., Hallett, J., 2009. A comprehensive habit diagram for atmospheric ice crystals: confirmation from the laboratory, AIRS II, and other field studies. J. Atmos. Sci. 61, 2888–2899. https://doi.org/10.1175/2009JAS2883.1.

Bailey, M., Hallett, J., 2012. Ice crystal linear growth rates from −20° to −70°C: confirmation from wave cloud studies. J. Atmos. Sci. 69, 390–402. https://doi.org/10.1175/JAS-D-11-035.1.

Bromwich, D.H., et al., 2012. Tropospheric clouds in Antarctica. Rev. Geophys. 50, RG1004 https://doi.org/10.1029/2011RG000363.

Cortes, C., Vapnik, V.N., 1995. Support-vector networks (PDF). Mach. Learn. 20 (3), 273–297. https://doi.org/10.1007/BF00994018.S2CID206787478. CiteSeerX 10.1.1.15.9362.

Cox, C.J., Noone, D.C., Berkelhammer, M., Shupe, M.D., Neff, W.D., Miller, N.B., Walden, V.P., Steffen, K., 2019. Supercooled liquid fogs over the central Greenland ice sheet. Atmos. Chem. Phys. 19, 7467–7485. https://doi.org/10.5194/acp-19-7467-2019.

Del Guasta, M., Vallar, E., Riviere, O., Castagnoli, F., Venturi, V., Morandi, M., 2012. Use of polarimetric LIDAR for the study of oriented ice plates in clouds. Appl. Opt. 45 (20), 4878–4887. https://doi.org/10.1364/AO.45.004878.

Del Guasta, M., 2022a. ICECAMERA: a flatbed scanner to study inland Antarctic polar precipitation. Atmos. Meas. Tech. 15, 6521–6544. https://doi.org/10.5194/amt-15-6521-2022.

Del Guasta, M., 2022b. CNN for the classification of ICECAMERA images of Antarctic ice particles. Zenodo. https://doi.org/10.5281/zenodo.6822140 [code].

Del Guasta, M., Ricaud, P., 2023. Dataset of in-situ and remote sensing measurements of precipitation in the inner Antarctic (Dome-C 75°S 123°E) for the years 2014-2021 (1.0). Zenodo. https://doi.org/10.5281/zenodo.8427614 [Data set].

Fridlind, A., nAtlas, R., van Diedenhoven, B., Um, J., Mcfarquhar, G., Ackerman, A., Moyer, E., Lawson, P., 2016. Derivation of physical and optical properties of midlatitude cirrus ice crystals for a size-resolved cloud microphysics model. Atmos. Chem. Phys. 16, 7251–7283. https://doi.org/10.5194/acp-16-7251-2016.

Fujita, K., Abe, O., 2006. Stable isotopes in daily precipitation at dome Fuji, East Antarctica. Geophys. Res. Lett. 33, L18503 https://doi.org/10.1029/2006GL026936.

Genthon, C., Six, D., Gallée, H., Grigioni, P., Pellegrini, A., 2016. Two years of atmospheric boundary layer observations on a 45-m tower at Dome C on the Antarctic plateau. J. Geophys. Res. Atmos. 118, 3218–3232. https://doi.org/10.1002/jgrd.50128.

Genthon, C., Veron, D., Vignon, E., Six, D., Dufresne, J.-L., Madeleine, J.-B., Sultan, E., Forget, F., 2021. 10 years of temperature and wind observation on a 45 m tower at Dome C, East Antarctic plateau. Earth Syst. Sci. Data 13, 5731–5746. https://doi.org/10.5194/essd-13-5731-2021.

Grazioli, J., Madeleine, J.-B., Gallée, H., Forbes, R.M., Genthon, C., Krinner, G., Berne, A., 2017a. Katabatic winds diminish precipitation contribution to the Antarctic ice mass balance. P. Natl. Acad. Sci. USA 114, 10858–10863. https://doi.org/10.1073/pnas.1707633114.

Grazioli, J., Genthon, C., Boudevillain, B., Duran-Alarcon, C., Del Guasta, M., Madeleine, J.-B., Berne, A., 2017b. Measurements of precipitation in dumont

d'Urville, adélie land, East Antarctica. Cryosphere 11, 1797–1811. https://doi.org/10.5194/tc-11-1797-2017.
Greenacre, M., 2018. Compositional data analysis in practice. https://doi.org/10.1201/9780429455537.
Gultepe, I., Kuhn, T., Pavolonis, M., Calvert, C., Gurka, J., Heymsfield, A.J., Liu, P., Zhou, B., Ware, R., Ferrier, B., Milbrandt, J., Bernstein, B., 2014. Ice fog in arctic during FRAM—Ice fog project: aviation and nowcasting applications. Bull. Am. Meteorol. Soc. 95 https://doi.org/10.1175/BAMS-D-11-00071.1.
Gultepe, I., Heymsfield, A.J., Field, P.R., Axisa, D., 2017. Ice-phase precipitation. Ch.6. Meteorol. Monogr. 58 https://doi.org/10.1175/AMSMONOGRAPHS-D-16-0013.1, 6.1-6.36. ISSN 0065-9401.
Gultepe, I., Heymsfield, A.J., Gallagher, M., 2020. Arctic ice fog: its microphysics and prediction. In: Kokhanovsky, A., Tomasi, C. (Eds.), Physics and Chemistry of the Arctic Atmosphere. Springer Polar Sciences, Springer, Cham. https://doi.org/10.1007/978-3-030-33566-3_6.
Heymsfield, A.J., Protat, A., Bouniol, D., Austin, R.T., Hogan, R.J., Delanoë, J., Okamoto, H., Sato, K., van Zadelhoff, G., Donovan, D.P., Wang, Z., 2008. Testing IWC retrieval methods using radar and ancillary measurements with in situ data. J. Appl. Meteorol. Climatol. 47 (1), 135–163. https://doi.org/10.1175/2007JAMC1606.1.
Hiley, M.J., Kulie, M.S., Bennartz, R., 2011. Uncertainty analysis for CloudSat snowfall retrievals. J. Appl. Meteorol. Climatol. 50 (2), 399–418. https://doi.org/10.1175/2010JAMC2505.1.
Hirasawa, N., Nakamura, H., Yamanouchi, T., 2000. Abrupt changes in meteorological conditions observed at an inland Antarctic Station in association with wintertime blocking. Geophys. Res. Lett. 27 (13), 1911–1914. https://doi.org/10.1029/1999GL011039.
Hogan, A.W., 1975. Summer ice crystal precipitation at the South Pole. J. Appl. Meteorol. 14 (2), 246–248. https://doi.org/10.1175/1520-0450(1975)014<0246:SICPAT>2.0.CO;2.
Hu, Y., Liu, Z., Winker, D., Vaughan, M., Noel, V., Bissonnette, L., McGill, M., 2006. Simple relation between LIDAR multiple scattering and depolarization for water clouds. Opt Lett. 31 (12), 1809. https://doi.org/10.1364/ol.31.001809.
Kameda, T., Fujita, K., Sugita, O., Hashida, G., 2007. Glaciological data collected by the 44th Japanese antarctic research expedition during 2003-2004. JARE data reports. Glaciology 32, 1–92. https://nipr.repo.nii.ac.jp/records/4997.
Kikuchi, K., Hogan, A.W., 1979. Properties of diamond dust type ice crystals observed in summer season at amundsen-scott south Pole station, Antarctica. J. of the Meteorol. Soc. of Japan. Ser. II 57 (2), 180–190. https://doi.org/10.2151/jmsj1965.57.2_180.
Kim, C.K., Stuefer, M., Schmitt, C.G., Heymsfield, A.J., Thompson, G., 2014. A numerical modeling of ice fog in Interior Alaska using weather research and forecasting model. Pure Appl. Geophys. https://doi.org/10.1007/s00024-013-0766-7.
Konishi, H., Muramoto, K., Shiina, T., Endoh, T., Kitano, K., 1992. Z-R relation for graupels and aggregates observed at Syowa station, Antarctica. Proc. NIPR Symp. Polar Meteorol. Glaciol. 5, 97–103. (Accessed 15 November 2023).
Kou, L., Lin, Z., Gao, H., Liao, S., Ding, P., 2023. Simulation and sensitivity analysis for cloud and precipitation measurements via spaceborne millimeter-wave radar. Atmos. Meas. Tech. 16, 1723–1744. https://doi.org/10.5194/amt-16-1723-2023.
Lachlan-Cope, T., Ladkin, R., Turner, J., Davison, P., 2001. Observations of cloud and precipitation particles on the avery plateau, antarctic peninsula. Antarct. Sci. 13 (3), 339–348. https://doi.org/10.1017/S0954102001000475.
Lawson, R.P., Baker, B.A., Zmarzly, P., O'Connor, D., Mo, Q., Gayet, J., Shcherbakov, V., 2006. Microphysical and optical properties of atmospheric ice crystals at south Pole station. J. Appl. Meteorol. Climatol. 45 (11), 1505–1524. https://doi.org/10.1175/JAM2421.1.
Lemonnier, F., Madeleine, J.-B., Claud, C., Genthon, C., Durán-Alarcón, C., Palerme, C., Berne, A., Souverijns, N., van Lipzig, N., Gorodetskaya, I.V., L'Ecuyer, T., Wood, N., 2019. Evaluation of CloudSat snowfall rate profiles by a comparison with in situ micro-rain radar observations in East Antarctica. Cryosphere 13, 943–954. https://doi.org/10.5194/tc-13-943-2019.
Listowski, C., Delanoë, J., Kirchgaessner, A., Lachlan-Cope, T., King, J., 2019. Antarctic clouds, supercooled liquid water and mixed phase, investigated with DARDAR: geographical and seasonal variations. Atmos. Chem. Phys. 19, 6771–6808. https://doi.org/10.5194/acp-19-6771-2019.
Liu, G., 2008. Deriving snow cloud characteristics from CloudSat observations. J. Geophys. Res. Atmos. 113, D00A09 https://doi.org/10.1029/2007JD009766.
Mace, G.G., Zhang, Q., Vaughan, M., Marchand, R., Stephens, G., Trepte, C., Winker, D., 2009. A description of hydrometeor layer occurrence statistics derived from the first year of merged CloudSat and CALIPSO data. J. Geophys. Res. 114, D00A26 https://doi.org/10.1029/2007JD009755.
Matrosov, S.Y., Heymsfield, A.J., 2017. Empirical relations between size parameters of ice hydrometeor populations and radar reflectivity. J. Appl. Meteorol. Climatol. 56, 2479–2488. https://doi.org/10.1175/JAMC-D-17-0076.1.
McFarquhar, G.M., Heymsfield, A.J., Spinhirne, J., Hart, B., 2000. Thin and subvisual tropopause tropical cirrus: observations and radiative impacts. J. Atmos. Sci. 57, 1841–1853. https://doi.org/10.1175/1520-0469(2000)057<1841:TASTTC>2.0.CO;2.
Ohtake, T., Yogi, T., 1979. Winter ice crystals at the South Pole. Antarct. J. U. S. 14, 201–203. (Accessed 1 November 2023).
Palerme, C., Kay, J.E., Genthon, C., L'Ecuyer, T., Wood, N.B., Claud, C., 2014. How much snow falls on the Antarctic ice sheet? Cryosphere 8, 1577–1587. https://doi.org/10.5194/tc-8-1577-2014.
Pincus, R., Aitchison, J., 1988. The Statistical Analysis of Compositional Data. Chapman and Hall, London - New York. https://doi.org/10.1002/bimj.4710300705, 1986, XII, 416 pp., Biom. J., 30: 794-794.
Platt, C.M.R., 1977. LIDAR observation of a mixed-phase altostratus cloud. J. Appl. Meteorol. Climatol. 16, 339–345. https://doi.org/10.1175/1520-0450(1977)016<0339:LOOAMP>2.0.CO;2.
Ricaud, P., Gabard, B., Derrien, S., Chaboureau, J.-P., Rose, T., Mombauer, A., Czekala, H., 2010a. HAMSTRAD-tropo, A 183-GHz radiometer dedicated to sound tropospheric water vapor over Concordia station, Antarctica. IEEE Trans. Geosci. Rem. Sens. 48, 1365–1380. https://doi.org/10.1109/TGRS.2009.2029345.
Ricaud, P., Gabard, B., Derrien, S., Attié, J.-L., Rose, T., Czekala, H., 2010b. Validation of tropospheric water vapor as measured by the 183-GHz HAMSTRAD Radiometer over the Pyrenees Mountains, France. IEEE Trans. Geosci. Rem. Sens. 48 (5), 2189–2203. https://doi.org/10.1109/TGRS.2009.2037920.
Ricaud, P., Genthon, C., Durand, P., Attié, J.-L., Carminati, F., Canut, G., Vanacker, J.-F., Moggio, L., Courcoux, Y., Pellegrini, A., Rose, T., 2012. Summer to winter diurnal variabilities of temperature and water vapor in the lowermost troposphere as observed by the HAMSTRAD radiometer over dome C, Antarctica. Bound-Layer Meteor 143, 227–259. https://doi.org/10.1007/s10546-011-9673-6.
Ricaud, P., Carminati, F., Courcoux, Y., Pellegrini, A., Attié, J.-L., El Amraoui, L., Abida, R., Genthon, C., August, T., Warner, J., 2014. Statistical analyses and correlation between tropospheric temperature and humidity at dome C, Antarctica. Antarct. Sci. 26, 290–308. https://doi.org/10.1017/S0954102013000564.
Ricaud, P., Del Guasta, M., Lupi, A., Roehrig, R., Bazile, E., Durand, P., Attié, J.-L., Nicosia, A., Grigioni, P., 2024. Supercooled liquid water clouds observed over Dome C, Antarctica: temperature sensitivity and cloud radiative forcing. Atmos. Chem. Phys. 24, 613–630. https://doi.org/10.5194/acp-24-613-2024.
Saito, M., Yang, P., 2016. Oriented ice crystals: a single-scattering property database for applications to LIDAR and optical phenomenon simulations. J. Atmos. Sci. 76, 2635–2652. https://doi.org/10.1175/JAS-D-19-0031.1, 2019.
Santachiara, G., Belosi, F., Prodi, F., 2016. Ice crystal precipitation at Dome C site (East Antarctica). Atmos. Res. 167, 108–117. https://doi.org/10.1016/j.atmosres.2015.08.006.
Satow, K., 1983. Observations on the shapes of snow crystals in the summer season in Mizuho plateau, Antarctica. Mem. Natl. Inst. Polar Res. - Special Issue 29, 103–109. (Accessed 5 November 2023).
Scarchilli, C., Frezzotti, M., Ruti, P.M., 2011. Snow precipitation at four ice core sites in East Antarctica: provenance, seasonality and blocking factors. Clim. Dynam. 37, 2107–2125. https://doi.org/10.1007/s00382-010-0946-4.
Schneider, U., Finger, P., Meyer-Christoffer, A., Rustemeier, E., Ziese, M., Becker, A., 2017. Evaluating the hydrological cycle over land using the newly-corrected precipitation Climatology from the global precipitation Climatology Centre (GPCC). Atmosphere 8, 52. https://doi.org/10.3390/atmos8030052, 2017.
Smiley, V.N., Whitcomb, B.M., Morley, B.M., Warburton, J.A., 1980. LIDAR determinations of atmospheric ice crystal layers at south Pole during clear-sky precipitation. J. Appl. Meteorol. 19 (9), 1074–1090. (Accessed 3 November 2023).
Sommer, M., von Rohden, C., Simeonov, T., Oelsner, P., Naebert, T., Romanens, G., Jauhiainen, H., Survo, P., Dirksen, R., 2023. GRUAN characterization and data processing of the Vaisala RS41 radiosonde. GRUAN Technical Document 8 (GRUAN-TD-8), v1.0.0 (2023-06-28). https://www.gruan.org/gruan/editor/documents/gruan/GRUAN-TD-8_RS41_v1.0.0_20230628_final.pdf.
Souverijns, N., Gossart, A., Lhermitte, S., Gorodetskaya, I.V., Grazioli, J., Berne, A., Duran-Alarcon, C., Boudevillain, B., Genthon, C., Scarchilli, C., van Lipzig, N.P.M., 2018. Evaluation of the CloudSat surface snowfall product over Antarctica using ground-based precipitation radars. Cryosphere 12, 3775–3789. https://doi.org/10.5194/tc-12-3775-2018.
Stenni, B., Scarchilli, C., Masson-Delmotte, V., Schlosser, E., Ciardini, V., Dreossi, G., Grigioni, P., Bonazza, M., Cagnati, A., Karlicek, D., Risi, C., Udisti, R., Valt, M., 2016. Three-year monitoring of stable isotopes of precipitation at Concordia Station, East Antarctica. Cryosphere 10, 2415–2428. https://doi.org/10.5194/tc-10-2415-2016.
Stephens, G.L., Vane, D.G., Boain, R.J., Mace, G.G., Sassen, K., Wang, Z., Illingworth, A.J., O'connor, E.J., et al., 2002. The Cloudsat mission and the A-Train. Bull. Am. Meteorol. Soc. 83, 1771–1790. https://doi.org/10.1175/BAMS-83-12-1771.
Stephens, G.L., Vane, D.G., Tanelli, S., Eastwood, Im, Durden, S., Rokey, M., Reinke, D., Partain, P., et al., 2008. CloudSat mission: performance and early science after the first year of operation. J. Geophys. Res. 113, D00A18 https://doi.org/10.1029/2008JD009982.
Trujillo-ortiz, A., Hernandez-Walls, R., Perez-Osuna, S., 2004. RAFISHER2CDA canonical discriminant analysis. https://doi.org/10.13140/RG.2.2.13024.10249.
Turner, J., Phillips, T., Thamban, M., Rahaman, W., Marshall, G.J., Wille, J.D., et al., 2019. The dominant role of extreme precipitation events in Antarctic snowfall variability. Geophys. Res. Lett. 46, 3502–3511. https://doi.org/10.1029/2018GL081517.
Um, J., McFarquhar, G.M., Hong, Y.P., Lee, S.-S., Jung, C.H., Lawson, R.P., Mo, Q., 2015. Dimensions and aspect ratios of natural ice crystals. Atmos. Chem. Phys. 15, 3933–3956. https://doi.org/10.5194/acp-15-3933-2015.
Vázquez-Martín, S., Kuhn, T., Eliasson, S., 2021. Shape dependence of snow crystal fall speed. Atmos. Chem. Phys. 21, 7545–7565. https://doi.org/10.5194/acp-21-7545-2021.
Vignon, É., Raillard, L., Genthon, C., Del Guasta, M., Heymsfield, A.J., Madeleine, J.-B., Berne, A., 2022. Ice fog observed at cirrus temperatures at Dome C, Antarctic Plateau. Atmos. Chem. Phys. 22, 12857–12872. https://doi.org/10.5194/acp-22-12857-2022.
Walden, V.P., Warren, S.G., Tuttle, E., 2003. Atmospheric ice crystals over the Antarctic plateau in winter. J. Appl. Meteorol. 42 (10), 1391–1405. https://doi.org/10.1175/1520-0450(2003)042<1391:AICOTA>2.0.CO;2.
Winker, D.M., Pelon, J.R., McCormick, M.P., 2003. The CALIPSO mission: spaceborne LIDAR for observation of aerosols and clouds. Proc. SPIE 4893. LIDAR Remote

Sensing for Industry and Environment Monitoring III, 1–11. https://doi.org/10.1117/12.466539.
Winker, D.M., Hunt, B.H., McGill, M.J., 2007. Initial performance assessment of CALIOP. Geophys. Res. Lett. 34, L19803 https://doi.org/10.1029/2007GL030135.
Wood, N., L'Ecuyer, T., Heymsfield, A., Stephens, G., 2015. Microphysical constraints on millimeter-wavelength scattering properties of snow particles. J. Appl. Meteorol. Climatol. 54, 909–931. https://doi.org/10.1175/JAMC-D-14-0137.1.